



Nanofibrous ϵ -polycaprolactone scaffolds containing Ag-doped magnetite nanoparticles: Physicochemical characterization and biological testing for wound dressing applications *in vitro* and *in vivo*

M.K. Ahmed^{a,b,*}, M.A. Zayed^c, S.I. El-dek^{d,**}, Mayssa Abdel Hady^e, Doaa H. El Sherbiny^{c,8}, Vuk Uskoković^{f,***}

^a Faculty of Nanotechnology for Postgraduate studies, Cairo University, El-Sheikh Zayed 12588, Egypt

^b Department of Physics, Faculty of Science, Suez University, Suez 43518, Egypt

^c Chemistry Department, Faculty of Science, Cairo University, 12613, Giza, Egypt

^d Materials Science and Nanotechnology Department, Faculty of Postgraduate Studies for Advanced Sciences, Beni-Suef University, Beni Suef, Egypt

^e Pharmaceutical Technology Department, National Research Centre, Dokki, Giza, Egypt

^f Advanced Materials and Nanobiotechnology Laboratory, TardigradeNano LLC, Irvine, CA, 92604, USA

⁸ Department of Biochemistry, Faculty of Dentistry, Modern University for Technology and Information, Mokattam, Cairo, Egypt

ARTICLE INFO

Keywords:

Tissue engineering
Wound healing
Skin
Magnetic nanoparticles
Nanofiber

ABSTRACT

Skin wounds can lead to numerous complications with dangerous health consequences. In this work, magnetite nanoparticles were doped with different concentrations of antimicrobial silver (Ag) ions and incorporated into the electrospun nanofibrous ϵ -polycaprolactone (PCL) scaffolds. Nanoparticles and scaffolds with various Ag contents were characterized using a range of physicochemical techniques. Ag entered magnetite as cations and preferentially positioned at tetrahedral sites, introducing lattice distortions and topographic irregularities. Amorphization of the structure due to accommodation of Ag expanded the lattice in the bulk and contracted it on the surface, where broadened distribution of Fe–O coordinations was detected. Promoting spin canting and diminishing the double exchange interaction through altered distribution of ferric and ferrous ions, Ag softened the magnetism of magnetite. By making the nanoparticle structure more defective, Ag modified the interface with the polymer and promoted the protrusion of the nanoparticles from the surface of the polymeric nanofibers, thus increasing their roughness and hydrophilicity, with positive repercussions on cell adhesion and growth. Both the viability of human melanocytes and the antibacterial activity against *E. coli* and *S. aureus* increased with the concentration of Ag in the magnetite phase of the scaffolds. Skin wound healing rate in rats also increased in direct proportion with the concentration of Ag in the magnetite phase, and no abnormalities in the dermal and epidermal tissues were visible on day 10 in the treatment group. These results imply an excellent potential of these composite nanofibrous scaffolds for use as wound dressings and in other reconstructive skin therapies.

1. Introduction

Skin is the largest organ of the body, acting as an essential physical and biological barrier against pathogens, toxins, irritants, allergens and other forms of adverse environmental stimuli [1,2]. It also plays a vital role in sensory functions and the internal homeostasis, alongside preventing the dehydration of internal tissues [3–5]. As a result, an injury to

the skin, such as through burns and other forms of trauma could entail a series of immune complications. Rapid healing is, therefore, vital for preventing the long-term damage to the organism in the case of such events and skin wound dressings are often used to replace portions of the lost skin and speed up its regeneration and healing [6–8]. Some of the essential properties that materials acting as candidates for skin wound dressings should have include biocompatibility, bioactivity, good

Peer review under responsibility of KeAi Communications Co., Ltd.

* Corresponding author. Faculty of Nanotechnology for Postgraduate Studies, Cairo University, El-Sheikh Zayed 12588, Egypt.

** Corresponding author.

*** Corresponding author.

E-mail addresses: m.khalaf@sci.suezuni.edu.eg (M.K. Ahmed), samaa@psas.bsui.edu.eg (S.I. El-dek), vuk21@yahoo.com (V. Uskoković).

<https://doi.org/10.1016/j.bioactmat.2020.12.026>

Received 28 September 2020; Received in revised form 24 December 2020; Accepted 25 December 2020

2452-199X/© 2021 The Authors. Production and hosting by Elsevier B.V. on behalf of KeAi Communications Co., Ltd. This is an open access article under the CC

BY-NC-ND license (<http://creativecommons.org/licenses/by-nc-nd/4.0/>).

integration with soft tissues, adequate mechanical properties and controllable biodegradation rate [9–11]. However, even when all of these requirements in a material are satisfied, reconstruction of the skin wound may be accompanied by bacterial infection, which could delay the healing process or even cause the regeneration failure [12–14]. Therefore, materials with intrinsic antibacterial properties are being intensely sought for wound dressing applications [15].

Biodegradable polymers have been the main materials of choice for applications in wound healing. Approved by the FDA, ϵ -polycaprolactone (PCL) presents one of the most commonly used biodegradable polymers [11,16,17]. It is particularly lauded for its good physical and biological properties, including biocompatibility, low degradation rate and good mechanical integrity. However, it displays a relatively high hydrophobicity, which limits its use as a pure phase.

Nanoparticles have attracted much attention because of their unique and tunable properties. Their differing in terms of physical and chemical properties compared to the corresponding bulk materials is primarily owing to high surface-to-volume ratios and the reactivity that this entails [18]. In some cases, nanoscale effects displayed by the nanoparticles are due to the high concentrations of crystallographic defects associated with the surface disorder; however, they can also be due to quantum resonance phenomena stemming from the similarity between the particle size and the critical lengths for particular physical effects [18]. Nanoparticles have been frequent additives in polymeric matrices, including PCL [19–21], with the goal of improving not only their mechanical strength, but also hydrophilicity, bioactivity and tissue bonding strength.

Magnetite has been one of the most intensely investigated materials for biomedical applications thanks to its strong magnetic properties and biocompatibility [22]. In particular, magnetite nanoparticles (MNPs) have made an outstanding contribution to biomedicine, as in the treatment of iron deficiencies, bio-imaging, biosensors, drug delivery, and magnetic hyperthermia [23]. Furthermore, like PCL, magnetite is also approved by the FDA [24], meaning that nanocomposites combining PCL and MNPs need no additional approvals before being tested in a clinical setting. Earlier, MNPs were used to deliver small molecules as facilitators of acute skin wound healing, such as thrombin [25] or curcumin [26], but this is the first study attempting to use MNPs not only as augmenters of cutaneous wound healing *per se*, but also as agents for the delivery of therapeutic ions to the skin wounds.

Magnetite is also a very common mineral. It is found in a number of igneous rocks and is also a major mineral component of many types of ore deposits [27]. Magnetite crystallizes in the inverse cubic spinel structure and contains both Fe^{2+} and Fe^{3+} ions, with the former occupying strictly the octahedral (B) sites and the latter occupying both the tetrahedral (A) and the octahedral (B) sites [28], resulting in the chemical formula of $\text{Fe}^{3+}[\text{Fe}^{3+}\text{Fe}^{2+}]\text{O}_4^{2-}$. Magnetite is ferromagnetic and its magnetic moment ($\sim 4\mu_{\text{B}}/\text{Fe}_3\text{O}_4$) is entirely due to the double exchange interaction and the larger $3d^6$ Fe^{2+} ions, with the nil contribution of the super-exchange interaction and smaller $3d^5$ Fe^{3+} ions. Through ionic substitution, many foreign cations (e.g., Ni^{2+} , Ti^{4+} , Co^{2+} , Al^{3+} , Mg^{2+} , Ga^{2+} , $\text{Mn}^{2+}/\text{Mn}^{4+}$, Cr^{2+} , Zn^{2+} , $\text{V}^{3+}/\text{V}^{4+}$) can be integrated into the crystal lattice of magnetite [29,30]. Through such doping as the intentional addition of appropriate ions into the host structure, desirable properties could be imparted on the parent material and its physicochemical characteristics improved [31].

For centuries, silver ions (Ag^+) released by silver compounds have been used for hygienic and healing purposes due to their antibacterial, antifungal and antiviral properties [32,33]. They have the capacity to strongly suppress the bacterial growth by inhibiting the respiratory enzyme pathways, restricting the electron transport chain components and directly interfering with DNA [34–37]. Compared to the delivery of Ag ions via Ag particles, their delivery as a dopant is anticipated to provide for slower release rates and thus avoid many of the adverse side effects associated with the use of particulate Ag as a biomaterial. Furthermore, silver nanoparticles exhibit a lower antibacterial activity

compared to the ionic form of silver and are vulnerable to oxidation, which may adversely modify the composite structure and disable the tuning effects enabled by the use of Ag as a dopant. Therefore, we surmise that the doping of MNPs with Ag ions may not diminish their biocompatibility while endowing them with an antibacterial activity, which they otherwise do not possess at considerable levels in the pure form [38,39].

Therefore, in this study, Ag-doped MNPs were incorporated inside the nanofibrous PCL scaffolds. Microstructural, crystallographic, spectroscopic and surface analyses were conducted to thoroughly understand the composition, structure and physicochemical properties of the resulting nanocomposites. To test the potential of the material for use as an antibacterial wound dressing, the viability and the attachment of human cells were analyzed in addition to the antibacterial activity *in vitro*, after which the capacity of the material to induce the healing of wounds to the skin was investigated *in vivo*, in the rat model. To meet the requirement for wound dressings, the materials are meant to mimic the structure of the extracellular matrix of the skin, which contains a relatively high porosity, particularly in the dermal area. This porous surface enables the transport of oxygen and nutrients, alongside promoting the vascularization and a proper blood supply to the healed tissue, through which the regeneration of the skin wound is accelerated. One of the most facile techniques for the production of such porous polymeric membranes is electrospinning. Electrospinning can be used to fabricate nanofibrous scaffolds with a controllable porosity, fiber diameter, distribution and orientation, and, thus, the strength. Thanks to their nanostructure, such scaffolds possess a high surface-to-volume ratio, which increases their bioactivity and the bonding strength with the host tissue. Their flexibility and moderate adhesiveness also allow for a particularly good contact with the skin. This nanofibrous structure permeated with sizable pores also allows for the entrapment of nanoparticles, which may improve specific properties of the material.

Consequently, the study has been underlain by the hypothesis that the entrapment of Ag-doped MNPs inside the electrospun PCL scaffolds would lead to a novel biomaterial for wound dressing applications. To that end, variation in the physicochemical properties of MNPs due to the addition of Ag ions and subsequent incorporation inside the PCL scaffold was investigated in the first stages of the study, whereas *in vitro* and *in vivo* biological response to the composite material containing different amounts of Ag in the MNP phase was investigated in the second stage. Combined, these experiments have allowed us to derive conclusions about the prospect of the material for clinical application.

2. Materials and methods

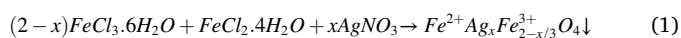
2.1. Materials

The analytical reagent grade of the materials used in the synthesis of MNPs was of the highest purity available. The chemicals used included ferrous chloride tetrahydrate, $\text{FeCl}_2 \cdot 4\text{H}_2\text{O}$ (99.9%) ($M_w = 198.81 \text{ g mol}^{-1}$), ferric chloride hexahydrate, $\text{FeCl}_3 \cdot 6\text{H}_2\text{O}$, (97.9%) ($M_w = 270.30 \text{ g mol}^{-1}$), ammonium hydroxide, NH_4OH (30%), silver nitrate, AgNO_3 (99.0% purity), hydrochloric acid, HCl ($M_w = 36.46 \text{ g mol}^{-1}$) with 98.0% purity, and ϵ -polycaprolactone (PCL, $M_w = 80,000 \text{ g mol}^{-1}$). All chemicals were purchased from Sigma Aldrich. Argon gas had the purity of 99.5%. Deionized water was used as a solvent.

2.2. Synthesis of magnetic nanoparticles (MNPs)

Ultrafine magnetite nanoparticles (Fe_3O_4 , MNPs) were synthesized using the co-precipitation technique. An aqueous solution containing $\text{FeCl}_3 \cdot 6\text{H}_2\text{O}$ and $\text{FeCl}_2 \cdot 4\text{H}_2\text{O}$ at the concentrations of 0.2 and 0.1 M, respectively, was prepared in 50 mL of deionized water and Ar gas was purged through it for 20 min. Then, ammonium hydroxide was added dropwise to the mixture at the rate of 2 mL/min. Meanwhile, the mixture was stirred using strong ultrasonic agitation (Ultrasonic probe

Sonicator, Thomas Scientific, 500 Watt) until the suspension became homogenous and the pH value of the solution reached 11.0 ± 0.1 . The inert gas was continuously bubbled through so as to prevent the formation of undesired oxides. The black precipitate was decanted from the solution with a permanent magnet and washed several times with deionized water and 10 times with ethanol to remove the excess ammonia and the residual ions from the precipitate. Then, the washed precipitate was dried at 50–60 °C for 12 h to obtain the black powder of magnetite. The Ag-doped samples were prepared by reducing the content of $\text{FeCl}_3 \cdot 6\text{H}_2\text{O}$ based on the following equation:



where $x = 0.0, 0.1$ and 0.2 yielded Ag-MNPs compositions named 0.0Ag-MNPs, 0.1Ag-MNPs and 0.2Ag-MNPs, respectively. The synthesis procedure is illustrated in Fig. 1.

To synthesize Ag-MNP-containing polymeric scaffolds, 110 mg of each Ag-MNP powder was added to 10 mL of PCL (8 wt%) in a sealed bottle and then the mixture was introduced into a high power probe sonicator for 15 min to obtain a well-dispersed suspension. Right after, these Ag-MNP-containing PCL solutions were introduced to a syringe pump to produced nanofibers via electrospinning. The electrospinning

system utilized the high voltage of 18 kV, the injection rate of 1 mL/h, and the distance between the needle and the collector wall of 16 cm.

2.3. Physicochemical characterization

2.3.1. XRD measurements

X-ray diffraction (XRD) analysis was carried out using an X-ray diffractometer (analytical-x' pertpro, Cu $k_{\alpha 1}$ radiation, $\lambda = 1.5404 \text{ \AA}$, 45 kV, 40 mA, Netherlands). The data were collected in the range of $4^\circ \leq 2\theta \leq 60^\circ$ with a step size of 0.02° and the irradiation time of 0.5 s per step.

The crystallite size in the polymeric phase was calculated using Scherrer's formula [40–42]:

$$D = \frac{k\lambda}{\beta_{\text{hkl}} \cos\theta} \quad (2)$$

where D refers to the crystallite size in nm, k represents the shape factor (0.9), λ is the wavelength of the X-rays (1.54056 \AA for CuK_{α} radiation), while β_{hkl} is the corrected full width at half maximum expressed in radians, and θ is the Bragg diffraction angle.

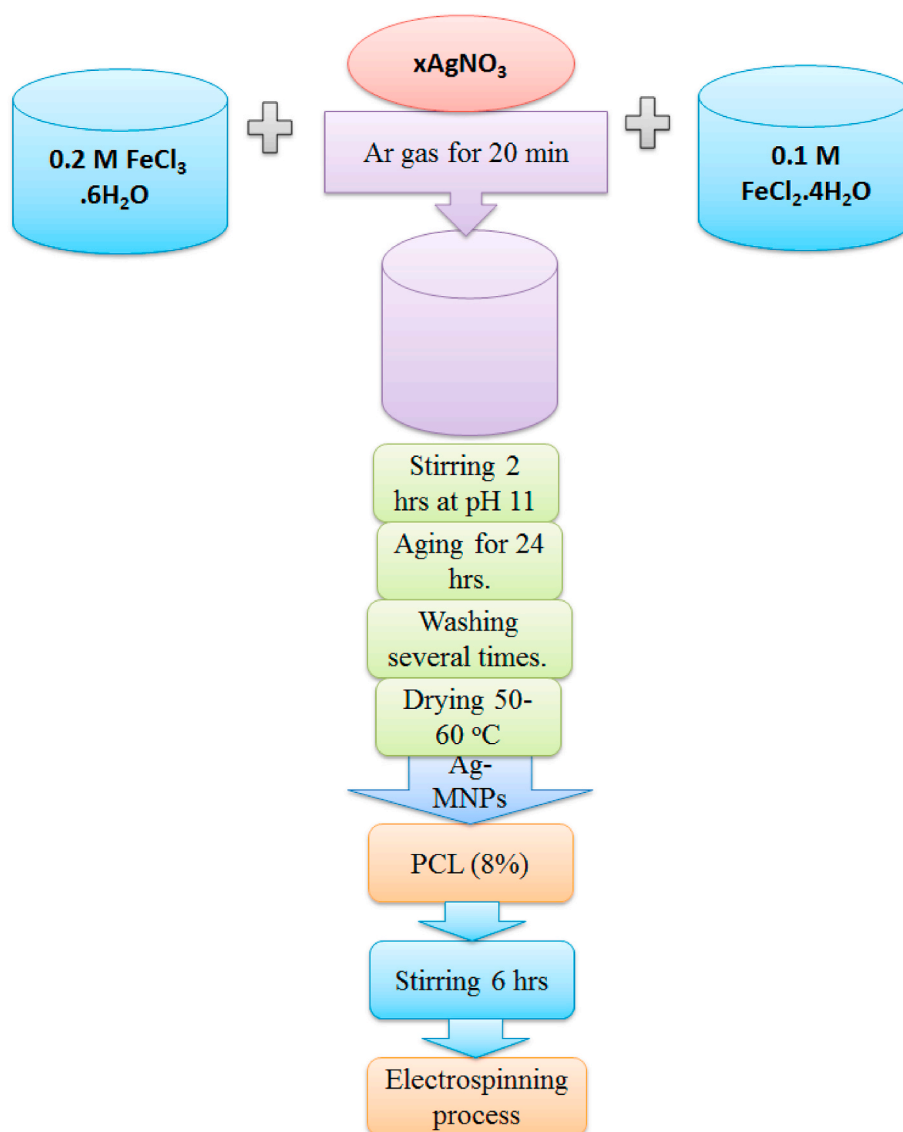


Fig. 1. Flow chart for the synthesis of MNPs doped with different concentrations of Ag ions, and their incorporation inside nanofibrous PCL scaffolds.

2.3.2. FTIR analyses

Fourier transformer Infrared (FTIR) spectra were recorded on a Perkin – Elmer 1650 spectrophotometer in the 4000–200 cm^{-1} wave-number region. The spectra were recorded using KBr pellets for the powder phase, while the nanofiber compositions were measured without additional KBr.

2.3.3. XPS measurements

X-ray photoelectron spectroscopy (XPS) analyses were conducted on pure and Ag-doped MNPs using a PerkinElmer PHI 5600 XPS instrument. Spherical sector was used as the analyzer type, while the multi-channel resistive plate was used as the detector. Analysis was performed in the constant pass energy mode with zero throughput and Al $K\alpha$ monochromatic radiation as the excitation source. Charge control was accomplished with an appropriately set emission current and electron energy. All samples were analyzed at room temperature.

2.3.4. Density and porosity

Porosity and real density were measured using a Quantachrome Instruments analyzer (UltraPyc 1200e). The analyses were done by processing a rectangular (2×3) cm area for each sample. Then the helium gas flowed through the cell and the averages of porosity and real density were derived from three independent measurements on each sample. The theoretical density (D_x) of Ag-MNPs could be estimated as [43]:

$$D_x = \frac{ZM}{NV} \quad (3)$$

Where M is the molecular weight of the fibers, N is Avogadro's number, Z is the number of molecules per unit cell, and V is the unit cell volume. However, the contribution of PCL must be taken into consideration and the total theoretical density can be represented as [44–47]:

$$TD_x = AD_{x1} + BD_{x2} \quad (4)$$

Where A and B represent the relative fractions of the two phases, Ag-MNPs and PCL, respectively, equaling $A = 12.09\%$ and $B = 87.91\%$. With PCL density being 1.145 g/cm^3 , the measured density is expressed in mass/volume units, while the total calculated porosity is given as a ratio between the theoretical and measured density (ρ) [48]:

$$P = \left(1 - \frac{\rho}{TD_x}\right) \times 100 \quad (5)$$

2.3.5. Morphological investigation

Field emission scanning electron microscope (FESEM) was used to scan the fibrous surfaces and assess the sample microstructures and morphologies under an operating voltage of 20–30 kV (model: QUANTA-FEG250, Netherlands). The powder phase was ground and carried on a piece of copper, before being sputtered with gold for 2 min. Further, a small piece of each nanofibrous scaffold was cut and sputtered with gold for 1 min to be ready for investigation.

2.3.6. Roughness measurements

Micrographs of nanofiber samples before being exposed to cells were obtained using FESEM and processed using the Gwyddion 2.45 software to investigate their roughness [44]. 3D micrographs were obtained for each sample and the resolution of the micrographs was fixed at 1450×900 pixels. The graphed edges were eliminated to avoid the unwanted boundaries. Finally, the roughness parameters were computed using the same software in nm. Roughness was measured for both the Ag-doped MNP powders and composite scaffolds. Each sample group was measured in triplicates so as to obtain the standard deviation.

2.3.7. Vibrating sample magnetometer (VSM)

Vibrating sample magnetometer (VSM, Model DMS 4HF) was used to measure the magnetic behavior of as-prepared powder samples.

2.3.8. Elemental analysis (ICP)

The elemental analysis was conducted for the MNP powder phase using an inductively coupled plasma (ICP) apparatus (720 ICP-OES, Agilent Technologies, USA). The sample preparation involved dissolving 0.01 g of each powder in 1 mL of HCL (33%) and adding 9 mL of deionized water.

2.3.9. Mechanical testing

The samples were processed into rectangular strips with the dimensions of $100 \times 20 \times 0.1$ mm. The stress/strain test was then carried out by pulling the nanofibers at the rate of 5 mm/min up to the fracture point, as in accordance with the standard code ASTM D882. Each sample group was measured in triplicates so as to obtain the standard deviation.

2.3.10. Contact angle measurements

Contact angles of the electrospun scaffolds were measured using the contact angle analyzer (OCA15EC, DataPhysics, Germany) at room temperature. Each sample group was measured in triplicates so as to obtain the standard deviation.

2.4. Biological characterization

2.4.1. In vitro cell viability tests

The human melanocyte cell line, HFB4, was cultured in Dulbecco's modified Eagle's medium (DMEM, Gibco) at 37°C and 5% CO_2 to investigate the viability of cells seeded onto the nanofibers. Cells seeded at the density of 5×10^3 cells/ cm^2 were cultured on the fibers in 12-well plates. After three days of incubation at 37°C , the medium was removed and MTT (3-(4,5-dimethylthiazol-2-yl)-2,5-diphenyltetrazolium bromide) was injected into each well, after which the cell viability was measured via an optical analyzer. Cell viability was defined as the percentage of the viable cells compared to the total cell number and it was measured in triplicates for each sample group so as to obtain the standard deviation [12–14]:

$$\text{Viability (\%)} = \frac{\text{Mean optical density of test samples}}{\text{Mean optical density of the control}} \times 100 \quad (6)$$

2.4.2. Cell growth on the scaffold

FESEM was used to observe the growth behavior of human melanocyte HFB4 cells seeded on the nanofibers. For this purpose, each sample was cropped into two pieces of 0.5×0.5 cm, which was then exposed to a UV lamp in 12 well plates for 30 min for sterilization. Then 1.5 mL of HFB4 cells (5×10^5 cells) were added into each well. Lastly, the plate was covered and incubated at 37°C for three days. After this time, the fibers were washed with phosphate buffer saline (PBS). To keep the cells fixed on the nanofiber surface, the scaffolds were submerged in a glutaraldehyde solution (2.5% concentration) for 1.0 h. They were then dehydrated in the air for 15 min. Finally, they were sputtered with gold for 2 min to be ready for FESEM imaging.

2.4.3. Antibacterial activity

The antibacterial activity was examined against both Gram-positive (*Staphylococcus aureus*) and Gram-negative (*Escherichia coli*) bacteria under the same conditions. The standard agar plate assay was used and the starting concentration of the powders was 50 mg/mL for each composition. The inhibition zone was measured in triplicates after 3 days of incubation at 37°C .

2.4.4. Wound healing assessment

A total of 8 albino rats were used for each sample group. The animals were classified to two sample groups: control and treated ones. The animals were almost 8 weeks old, weighed 250 g each, and were individually kept in clean polyethylene cages under the standard experimental conditions and the temperature of $25 \pm 2^\circ\text{C}$. Rats were prepared for experiments in different stages. First, they were anesthetized with

intra-peritoneal ketamine and xylazine injections with a dosage of 0.2 mL/100 g body weight. After shaving and sterilization with 70% ethanol, full thickness wounds were made on the dorsal surface using a sterile cylindrical stainless-steel rod with 5 mm in diameter and biopsies were sent for a histological analysis. Size, morphology and the depth of the wounds were investigated.

The wounds were covered with the nanofibrous scaffolds and then with the cotton gauze. After the dressing materials were applied, the rats were housed individually in cages under the normal room temperature. Observations were done daily for ten days. Rats were fed using the commercial pellets and water, *ad libitum* throughout the study stage. The

assessed wound healing parameters were carried out via monitoring the measurement of the cut edge contraction, continuously observing for possible signs of bacterial infection and analyzing histopathological findings of the wound skin autopsy after ten days of treatment. Measurements of the wound area and changes in the wound edge diameter were measured in mm using a digital caliper daily before and after the treatment. The wound edge contraction was expressed as a decrease of the original wound diameter. All measurements were recorded for further statistical analyses. Animal experiments were performed at the National Research Centre, Dokki, Giza, Egypt, with the compliance with all relevant ethical regulations.

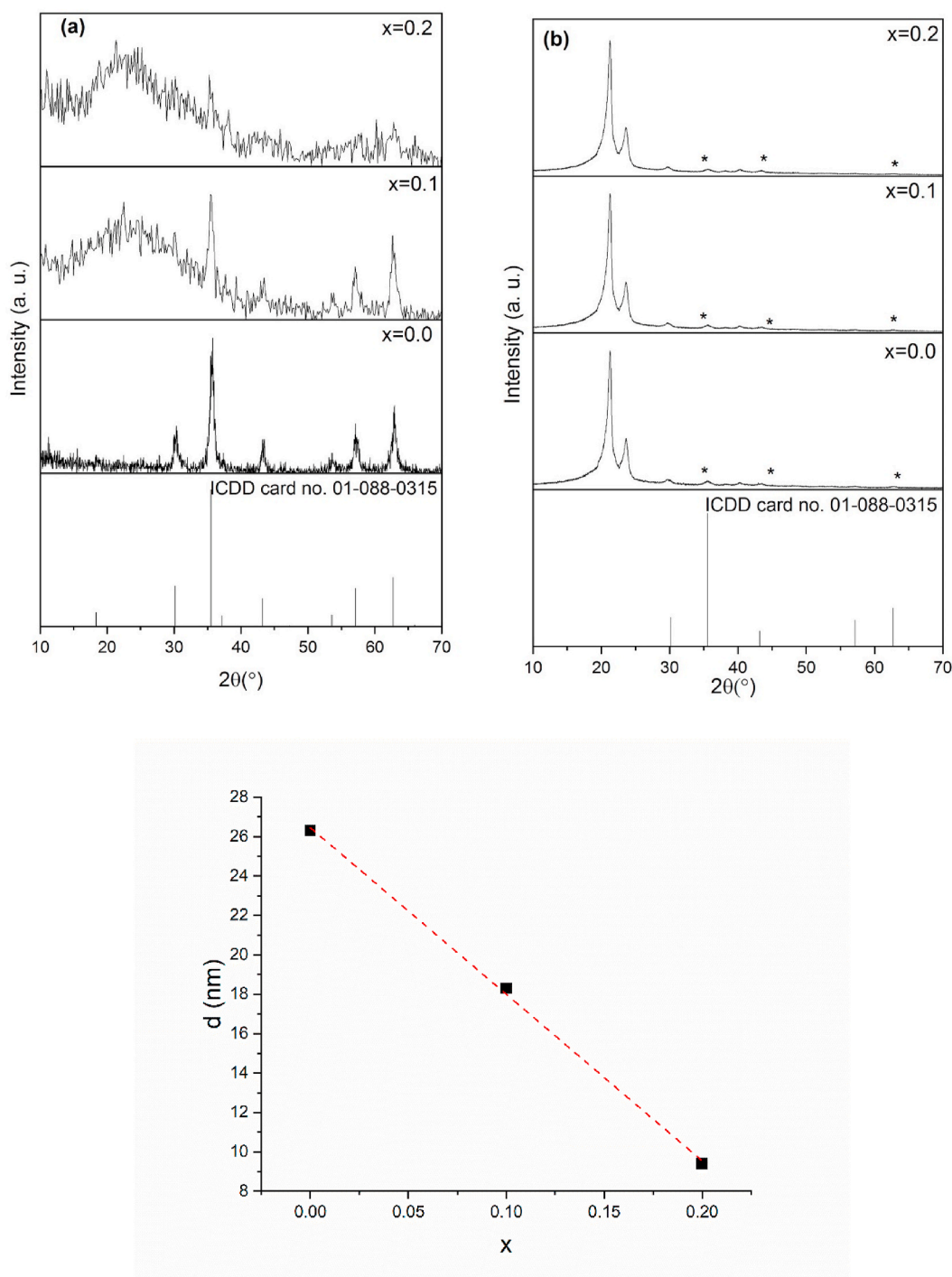


Fig. 2(a, b). XRD patterns for Ag-MNPs powders (a) and Ag-MNPs@PCL nanofibers (b) with different concentrations of Ag in the MN phase, along with the linear dependence of the average crystallite size of x Ag-MNP on the stoichiometric parameter x .

2.4.5. Histological analysis

The rats were euthanized at the end of the study period (10 days). The skins were fixed in 10% formalin for 24 h, dehydrated in a graded ethanol series, and then embedded in paraffin. Specimens were embedded in paraffin beeswax to form tissue blocks. The blocks were then cut into 5 μm sections with 4 μm thicknesses using a microtome, deparaffinized and stained with hematoxylin and eosin as well as Alizarin Red. After the staining, the sections were examined under the optical microscope.

3. Result and discussion

3.1. Structural analysis

The crystal structure analysis of both Ag-MNPs and Ag-MNP-containing PCL nanofibers (Ag-MNPs@PCL) was carried out using XRD and the results are presented in Fig. 2 and Table 1.

XRD patterns demonstrated that magnetite formed as a single phase with the cubic symmetry conforming to the ICDD card no. 01-088-0315. XRD reflections of MNPs displayed intense broadening as the concentration of Ag in them increased. Along with the formation of the low-angle hump centered at $2\theta \sim 20\text{--}25^\circ$ and characteristic of amorphous magnetite [49], this signified intense lattice distortions and reduced crystallinity due to the accommodation of Ag ions (Fig. 2(a)). As a result, the average crystallite size estimated using the Scherrer's equation decreased from 26.3 nm for 0.0Ag-MNPs to 18.3 ± 4.1 nm for 0.1Ag-MNPs to 9.4 ± 2.4 nm for the highest concentration of Ag in Ag-MNPs, namely 0.2Ag-MNPs (Table 1). The trend of change in the crystallite size, d , with the content of Ag defined by the stoichiometric parameter x was linear, with the goodness of the fit of $R^2 = 0.99906$, and could be predicted using the following formula: $d = 26.45 - 84.5x$ ($0 \leq x \leq 0.2$) (Fig. 2(c)). This constancy of the change in crystallinity is also an excellent predictor of the success of incorporation of Ag ions into magnetite crystals. During this process, the lattice parameter a increased from 8.355 ± 0.050 up to 8.364 ± 0.090 Å, while the unit cell volume rose from 583.258 ± 2.120 to 585.014 ± 3.870 Å³ for 0.0Ag-MNPs and 0.2Ag-MNPs, respectively. This expansion of the unit cell length and volume accompanies the distortion of the crystal structure, conforming to the typical increase in the average bond lengths as a crystalline structure transforms to an amorphous one. This transformation is expected to lead to changes in the morphological characteristics and the reduction of magnetization.

In contrast to the intense changes that the XRD patterns of MNPs underwent with changes in the Ag concentration, no such changes were detected in the XRD patterns of MNPs@PCL. All of these diffractograms, with or without Ag in the MNP phase, displayed the dominance of the two most prominent diffraction peaks originating from semi-crystalline PCL, namely (110) at $2\theta \sim 22^\circ$ and (200) at $2\theta \sim 24^\circ$.

3.2. FT-IR analyses

Fig. 3 shows the FT-IR spectra obtained on Ag-MNP powders (Fig. 3(a)) and Ag-MNPs@PCL nanofibers (Fig. 3(b)) containing different Ag

Table 1

Crystallographic data for MNPs doped with different concentrations of the Ag ion, including crystallite size, the lattice parameter a , the unit cell volume (V), the theoretical density (D_x), the measured density (ρ), and the porosity ratio (P).

Composition	Crystallite size (nm)	a (Å)	V (Å ³)	D_x (g/cm ³)	ρ (g/cm ³)	P (%)
0.0Ag-MNPs	26.3 ± 3.4	8.355	583.258	5.50	2.96	46.3
		± 0.05	± 2.12	± 0.8	± 0.2	± 4.5
0.1Ag-MNPs	18.3 ± 4.1	8.363	585.196	5.37	2.65	50.7
		± 0.07	± 3.32	± 0.6	± 0.4	± 5.8
0.2Ag-MNPs	9.4 ± 2.4	8.364	585.014	5.26	$3.5 \pm$	33.4
		± 0.09	± 3.87	± 0.7	0.3	± 4.5

concentrations in the MNP phase in the range of 4000–500 cm^{-1} . The most characteristic band for magnetite is detected at 443.3–578.7 cm^{-1} and is associated with the stretching vibrational mode of Fe–O bonds in iron oxides [50]. This band was consistently present in MNPs doped with different concentrations of Ag ions, confirming the presence of the same magnetite phase in all the samples, regardless of whether they were doped with Ag or not.

The broad band covering the 3200–3700 cm^{-1} range in the spectra of Ag-MNPs was due to the symmetric and antisymmetric stretching O–H vibrations of water absorbed on the surface of the NPs. Despite the more porous structure of the composite material, which can accommodate large amounts of adsorbed water, this signature water band was absent in the spectra of Ag-MNPs@PCL nanofibers, confirming the aforementioned less hydrophilic and less hygroscopic nature of PCL compared to MNPs. Another water band prominent in the spectra of Ag-MNPs and absent in the spectra of Ag-MNPs@PCL peaked at 1633 cm^{-1} , originating from the bending mode of H–O–H. These water modes are frequently detected in MNPs spectra [51,52], where they indicate both the hydroxyl groups forming in place of oxides on the NP surface and the adsorbed water. In spite of the multiple steps of washing with alcohol during the synthesis of Ag-MNPs, these O–H bands were over the detection limit of FT-IR, indicating the highly hydrophilic nature of the NPs. Still, the integrated intensity of both water bands, namely the stretch at 3200–3700 cm^{-1} and the bend at 1620–1640 cm^{-1} , increased with the addition of Ag, which is due to the increase in the hygroscopic nature of magnetite with the addition of Ag ions to it. Further, it can be noticed that the Fe–O band detected at 443.3 cm^{-1} in the case of 0.2Ag-MNPs got upshifted to 454.4 cm^{-1} for 0.2Ag-MNPs@PCL. This shift can be explained by the better dispersion of the MNPs when they are incorporated within the PCL scaffold than when they form a powder. Namely, in the powder form, particles aggregate and each Fe–O bond on average experiences a larger pull due to being surrounded by other bonds of the same type, which lowers the vibration mode frequency compared to that exhibited by particles dispersed better in a medium.

The FT-IR spectra of the composite nanofibers expectedly contained a higher density of bands compared to the spectra of Ag-MNPs. The characteristic bands of the polymeric phase in Ag-MNPs@PCL nanofibers are reported in Table 2. The most prominent of them was the C=O stretch at 1723.5 cm^{-1} followed by the C–O–C stretch at 1163–1165 cm^{-1} and the C–H stretch at 2863–2865 cm^{-1} (Fig. 3).

3.3. XPS spectra

To characterize the surface bond structure of as-synthesized MNPs and 0.2Ag-MNPs, the individual spin-orbital components of the Fe 2p, O 1s and Ag 3d spectral lines in the raw XPS spectra were deconvoluted into subcomponents, as illustrated in Fig. 4(a–d) and in Table 3.

The binding energies of 710.6 and 713.87 eV correspond to the core level Fe 2p_{3/2} lines in the XPS spectrum of pure magnetite [63–65], while the Fe 2p_{1/2} lines were upshifted by ~ 12 eV (Table 3).

Here, while Fe 2p_{3/2} denotes Fe³⁺ in the octahedral (B) sites, Fe 2p_{1/2} denotes Fe³⁺ at the tetrahedral (A) sites [73]. The difference in the upshift of the Fe 2p_{1/2} line compared to the Fe 2p_{3/2} line was 13.02 eV in the spectrum of 0.0Ag-MNPs and 13.67 eV in the spectrum of 0.2Ag-MNPs. However, the Fe 2p_{3/2} vs. Fe 2p_{1/2} intensity ratio increased with the introduction of Ag into MNPs, suggesting that the Fe³⁺ ions were replaced from the tetrahedral sites to the octahedral sites by the incoming Ag ions, as in accordance with the stoichiometric formula $\text{Ag}_x\text{Fe}_{(1-x)/3}^{3+}[\text{Fe}^{3+}\text{Fe}^{2+}]_2\text{O}_4^-$. Given that the radius of the Ag⁺ cation (115 p.m.) lies closer to that of the ferrous, Fe²⁺ ion (78 p.m.) than to that of the ferric, Fe³⁺ ion (64 p.m.), the most probable reason for the preferential accommodation of Ag at the tetrahedral sites solely occupied by the Fe³⁺ ions lies in the lower oxygen coordination of cations at these sites compared to that at the octahedral sites. Moreover, the splitting of each of the two Fe 2p lines was more symmetric and in favor of the higher energy doublet component with the addition of Ag. Similarly,

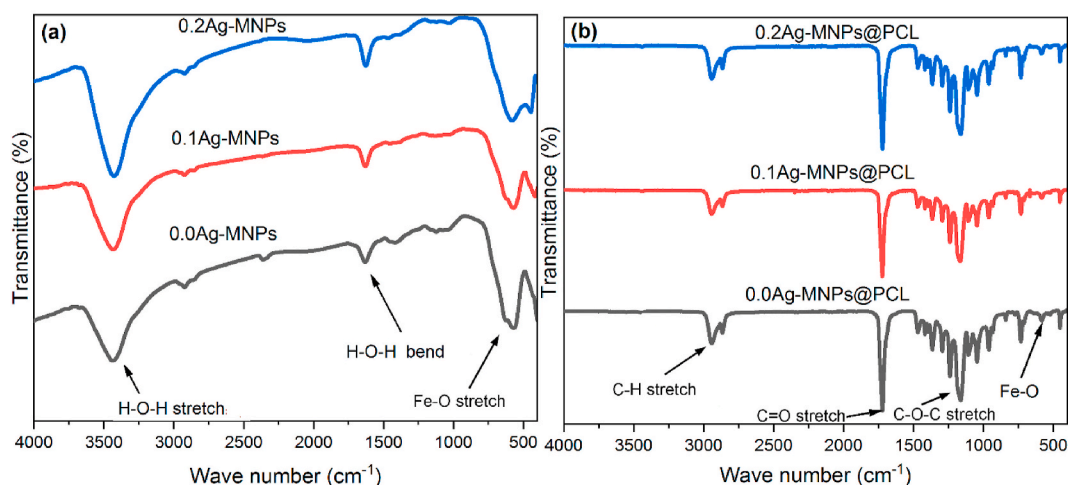


Fig. 3. FTIR spectra of Ag-MNPs powders (a) and Ag-MNPs@PCL nanofibers (b) with different concentrations of Ag in the MN phase.

Table 2

Characteristic FT-IR bands for Ag-MNPs and Ag-MNPs@PCL nanofibers at different concentrations of Ag ions.

Ag-MNPs			Ag-MNPs@PCL			Assignment	Ref
x = 0.0	x = 0.1	x = 0.2	x = 0.0	x = 0.1	x = 0.2		
–	–	443.3	451.8	456.1	454.4	Fe–O	[50,53]
569.4	567.7	578.7	583	583	583.1		
–	–	–	1164.8	1163.5	1163.1	C–O–C stretching vibrations	[54]
–	–	–	1242.3	1239.7	1236.3		
–	–	–	1297.7	1298.7	1300.2	C–O and C–C stretching	[55]
–	–	–	1365.2	1367.5	1361.8	stretching of CH ₂ and OH group	[56]
–	–	–	1471.7	1473.1	1472.1		
–	–	–	1723.5	1723.6	1723.5	C=O	[21,57]
1628.1	1635.1	1623.3	–	–	–	H–O–H bending	[21,57]
2356.4	–	–	2863.2	2865	2864.8	stretching mode of C–H	[58,59]
2916.1	2920.3	2929.7	2940.9	2940.8	2940.1		
3436.5	3440.8	3425.5	–	–	–	H–O–H stretching	[60–62]

most Fe 2p lines increased in energy with the addition of Ag. Amorphization of the structure accompanying the addition of Ag is a process during which the bonds distort and extend on average, thus lowering the binding energy of core electrons; however, this effect cannot be explained by the results of the XPS analysis. Although it may still apply to the bulk of the structure, it does not apply to the surface as well. There, a different effect occurs, primarily related to the lattice compaction due to bond under-saturation. During this process, amorphization still occurs due to the presence of Ag ions and is accompanied by a broadened distribution of coordination numbers and types. This effect is confirmed by the increase in the fine structure of the O 1s line upon the addition of Ag ions to MNPs. Thus, while pure MNPs displayed a major Fe–O component and a minor Fe–OH component, the 0.2Ag-MNPs sample displayed a significantly more intense Fe–OH component along with the Fe–O–OH one. And another unidentified one, the latter two of which were absent in the XPS spectrum of 0.0Ag-MNPs. A distinct shake-up satellite peak was detected in-between the two spin-orbital components of the Fe 2p line, at 718.62 eV in pure MNPs, which is indicative of Fe³⁺ ions in the configuration of maghemite (γ -Fe₂O₃). This has suggested a finite presence of maghemite on the MNP surface. Interestingly, the addition of Ag caused the splitting of this satellite peak to two equally intense components, possibly suggesting the presence of iron in two different Fe₂O₃ configurations on the surface. Finally, the typical splitting of the Ag 3d binding energy region to separate spin-orbital components [35] was estimated to be 5.85 eV, very near the typical 6.0 eV separation in the metal. However, together with the relatively broad nature of the peaks, no observed minor loss features at ~2 eV upshifts from both Ag 3d_{3/2} and 3d_{5/2} components and no low energy component at ~365 eV after the deconvolution indicated that no

metallic clusters of Ag formed in the system and that all Ag species were cationic in nature and incorporated into the lattice of MNPs. It is conceivable that metallic clusters would form at higher concentrations of Ag than x = 0.2. However, within the concentration range utilized in this study, no such clusters were detected. This is in agreement with the intense effects Ag ions had on the crystallinity of the material, an effect that could be exhibited only due to the direct incorporation of Ag ions into the lattice of MNPs.

3.4. ICP measurement

To verify the presence of Ag in Ag-MNPs and compare its concentration with the theoretical, chemical investigation was done using ICP. The results displayed in Table 4 show that the theoretical values increase from 0.0 to 4.55–8.10 ppm for 0.0Ag-MNPs, 0.1Ag-MNPs and 0.2Ag-MNPs, respectively, whereas somewhat higher values of 6.00 ± 0.12 and 8.60 ± 0.32 ppm for 0.1Ag-MNPs and 0.2Ag-MNPs, respectively, were measured in the synthesized powders, suggesting that the precipitation of Ag ions proceeds more completely than that of Fe ions, an effect that is likely associated with the lesser hydration enthalpy of the former ions. The close values further suggest that Ag ions were entirely captured by the MNPs during their co-precipitation. Such good capture capacity allows for fabricating Ag-MNP compositions with high accuracy at relatively low Ag contents such as those used in this study.

3.5. Magnetic properties

The response of a magnetic material in the magnetic field depends strongly on its cation distribution, chemical composition, crystal

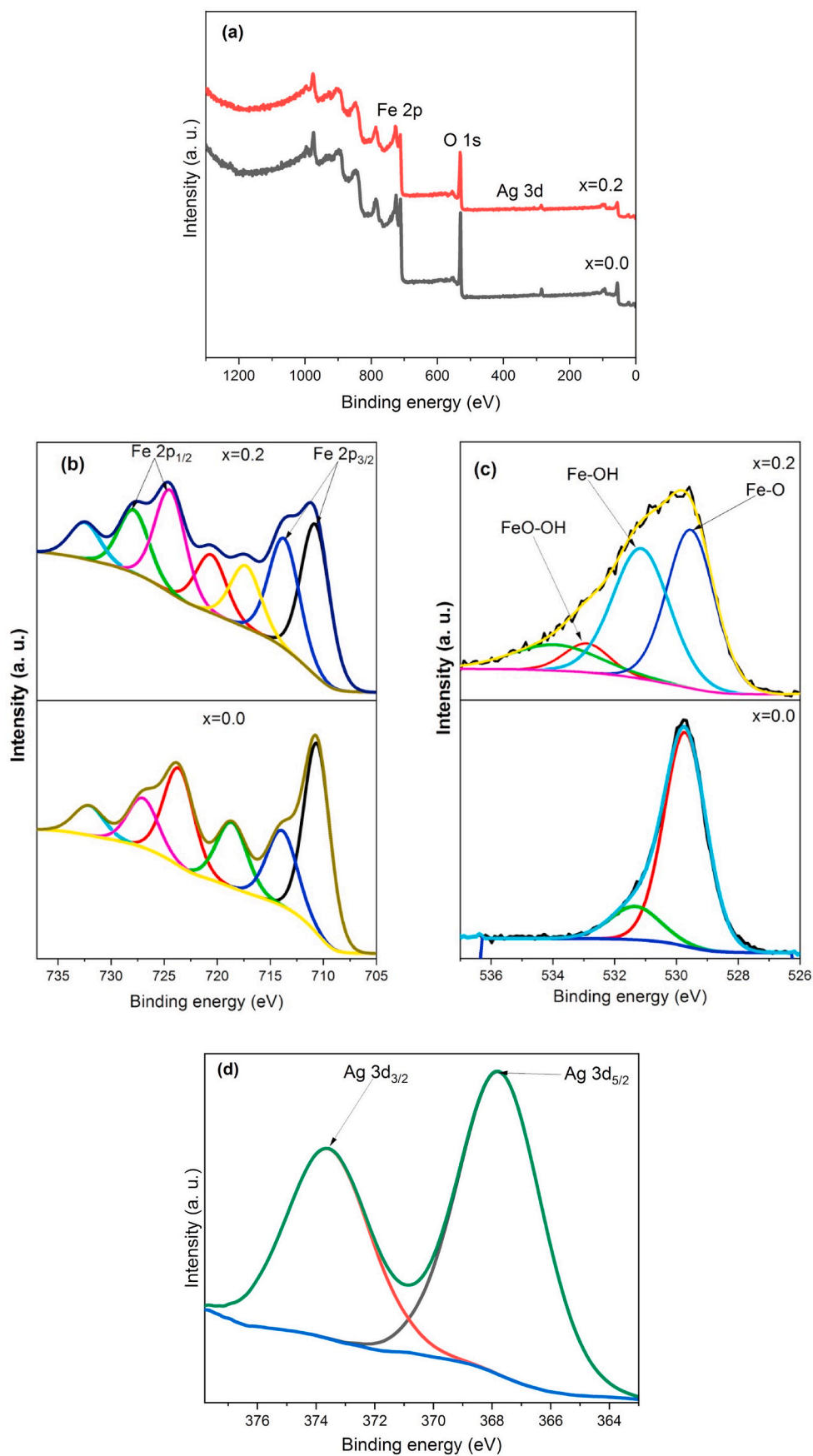


Fig. 4. Comparative XPS spectra of MNPs (0.0Ag-MNPs) and MNPs doped with the highest concentration of the Ag ions (0.2Ag-MNPs): (a) survey scan, (b) Fe 2p region, (c) O 1s region, and (d) Ag 3d region.

Table 3
Characteristic XPS peaks for Ag-MNPs at different concentrations of the Ag ion.

x	Bond	Binding energy (eV)	Atomic (%)	Assignment	Ref	
0.0	Fe2p	710.6	33.99	Fe 2p _{3/2}	[66,67]	
		713.87	15.58	Fe 2p _{3/2}	[68]	
		718.62	13.53	Fe ³⁺	[69]	
		723.62	20.33	Fe 2p _{1/2}	[66,67]	
		726.99	10.31	Fe 2p _{1/2}	[68]	
	732.09	6.25				
	O1s	529.72	84.28	Fe–O	[70,71]	
		531.34	15.72	Fe–OH	[66]	
	0.2	Fe2p	710.76	24.62	Fe 2p _{3/2}	[66,67]
			713.69	19.03	Fe 2p _{3/2}	[68]
717.31			10.76	Fe ³⁺	[69]	
720.57			10.13	Fe ³⁺	[69]	
724.43			17.98	Fe 2p _{1/2}	[66,67]	
727.86		11.04	Fe 2p _{1/2}	[68]		
732.46		6.44				
O1s		529.54	40.71	Fe–O	[70,71]	
		531.14	39.98	Fe–OH	[70]	
		532.9	7.01	FeO–OH	[70]	
Ag3d	533.93	12.3				
	367.73	61.41	Ag 3d _{5/2}	[72]		
	373.58	38.59	Ag 3d _{3/2}	[72]		

Table 4

A comparison between the measured (W_{exp}) and the theoretical (W_t) content of Ag in Ag-MNPs derived from the ICP analysis.

Composition	W_{exp} [ppm]	W_t [ppm]
0.0Ag-MNPs	0.0 ± 0.0	0.0 ± 0.0
0.1Ag-MNPs	6.0 ± 0.12	4.55 ± 0.21
0.2Ag-MNPs	8.6 ± 0.32	8.1 ± 0.32

arrangement and crystallinity beside preparation conditions. The magnetic properties of the prepared nanomaterials varied significantly with the incorporation of Ag ions, as it is illustrated in Fig. 5.

Table 5 additionally reports the main magnetic parameters derived from the hysteresis loops ($M-H$). All materials evidently displayed the ferromagnetic response in the magnetic field, which is typified by the residual magnetization at $H = 0$, finite coercivity and considerable saturation magnetization [74,75]. Specific saturation magnetization (M_s), however, decreased drastically with the addition of Ag, from 103.1 to 85.1 to 32.3 emu/g for 0.0Ag-MNPs, 0.1Ag-MNPs and 0.2Ag-MNPs, respectively, and the remnant magnetization (M_r) followed the same

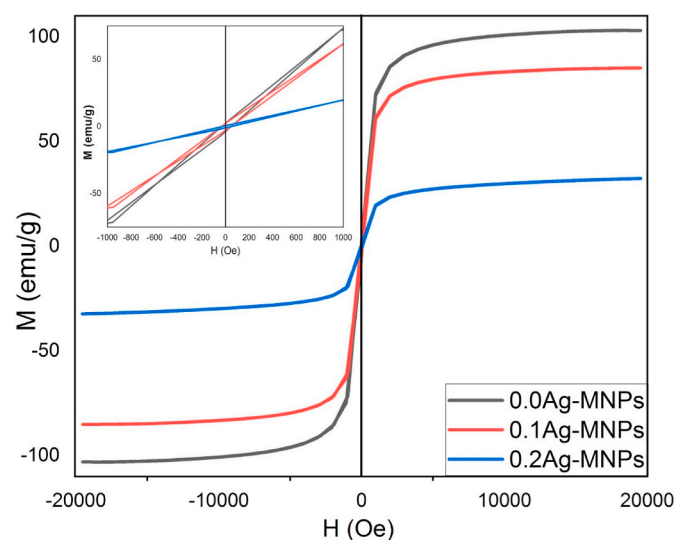


Fig. 5. Hysteresis loops ($M-H$) for MNPs doped with different concentrations of Ag ions.

trend (Table 4). This reduction in magnetization can be explained partly by the substitution of Fe^{2+} ions by the Ag ions. Namely, with the reduction of the number of magnetic dipole carriers in the material, its effective magnetic moment naturally drops. However, this simple ionic substitution effect alone cannot explain for the exponential drop in magnetization with an increase in the amount of Ag ions in MNPs. Another major effect causing reduced magnetization is that of the spin canting becoming prevalent in the spinel crystal structure of MNPs disordered by the presence of Ag dopants. Finally, the third major effect comes from the aforementioned preferential accommodation of Ag ions at the tetrahedral sites of the spinel lattice, from which they expel Fe^{3+} ions and shift them to the octahedral sites. One effect of the accommodation of Ag at the tetrahedral sites and the replacement of the Fe^{3+} ions to the octahedral sites is reduced concentration of Fe^{2+} ions at these octahedral positions. As mentioned earlier, Fe^{2+} ions are the sole carriers of magnetism in magnetite, there are two types of magnetic dipole coupling in the magnetite structure: super-exchange interaction and double-exchange interaction. The former involves an antiferromagnetic interaction between an octahedral Fe^{3+} ion ($Fe^{3+}(B)$) and a tetrahedral Fe^{3+} ion ($Fe^{3+}(A)$) mediated by the 2p orbitals of the O^{2-} anion and representable as $Fe^{3+}(B)\uparrow O^{2-}\uparrow Fe^{3+}(B)\downarrow$. Here, the spins of the 5d electrons of the Fe^{3+} ions on the opposite ends of the super-exchange interaction compensate for each other's spin dipole moments, resulting in zero net magnetization. The second type of interaction, the double-exchange interaction, involves the hopping of an electron with an unpaired spin from $Fe^{2+}(B)$ to $Fe^{3+}(A)$ and results in coupled spins that are aligned parallel, in which case only Fe^{2+} cations contribute to the effective magnetic moment of the material. However, with the diminishment of the Fe^{2+} centers caused by the addition of Ag ions, the double-exchange interaction gets weakened and the magnetization reduced. This preferential accommodation of nonmagnetic Ag^+ ions at the tetrahedral position and the resulting expulsion of Fe^{3+} ions to the octahedral site was previously reported to have caused a decrease in the magnetic moment of the material [76–78]. The same effect leads to an observable deterioration of magnetization upon the addition of Ag^+ to MNPs. The magnetic moment (μ) can be represented as follows:

$$\mu = \frac{[M_w \times M_s]}{[N_A \times \mu_B]} \quad (7)$$

where M_w refers to the molecular weight, N_A is the Avogadro number, and $N_A \times \mu_B = 5585$. The magnetic moments calculated from this expression were 0.947 μ_B , 0.967 μ_B and 0.828 μ_B for $x = 0.0$, 0.1 and 0.2, respectively. As for other magnetic properties measured, the exchange bias (H_{EB}) of the applied field could be measured as [79]:

$$H_{EB} = \frac{-[H(-) + H(+)]}{2} \quad (8)$$

where $H(-)$ and $H(+)$ denote the magnetization intercepts with the $-ve$ and $+ve$ positions on the applied field axis. H_{EB} decreased with the addition of Ag, but then got restored with the further addition of Ag. In contrast, coercivity (H_c) values were within the same range of values for all the compositions. However, with H_c more or less constant and M_s inversely proportional to the concentration of Ag, the hysteresis loop area exhibited a steady drop together with the M_s values indicating the softening of magnetism that proceeded in direct proportion with the addition of Ag.

All in all, Ag ions are shown to preferentially position at the tetrahedral sites of the spinel lattice, thereby altering the distribution of ferric and ferrous ions and diminishing the double exchange interaction. Together with spin canting caused by the induced crystallographic defects in the structure, the presence of Ag thus softens the magnetism and significantly reduces the magnetic moment of pure magnetite, which exceeded 100 emu/g. It is, however, uncertain how this reduction in the magnetic moment may affect the biological response of the material. It is likely that other properties, including hydrophilicity, crystallinity and

Table 5

Magnetic properties of pure MNPs and MNPs doped with different amounts of Ag ions, including positive and negative saturation magnetization (M_s), remanence (M_r), coercive field (H_c), the ratio of remnant magnetization to saturation magnetization (M_r/M_s), the exchange bias field (H_{EB}), and the hysteresis loop area.

Composition	M_s (+) emu/g	M_s (-) emu/g	M_r (+) emu/g	M_r (-) emu/g	H_c (+) (Oe)	H_c (-) (Oe)	H_{EB} (Oe)	Area erg/g $\times 10^3$
0.0Ag-MNPs	103.09	-103.09	3.72	-3.10	48.15	-32.04	8.055	8.64
0.1Ag-MNPs	85.12	-85.12	2.83	-2.54	43.85	-34.21	4.82	7.31
0.2Ag-MNPs	32.29	-32.29	0.99	-0.80	47.80	-29.21	9.295	2.77

topography, present more decisive determinants of this response.

3.6. Morphological features of MNPs and Ag-MNPs

Fig. 6(a–f) shows the morphological effects of the addition of substitutional Ag ions to MNPs. Pure MNPs took the form of agglomerated grains with the dimensions of around 2.5 μm . The grains of 0.1Ag-MNPs possessed a wide range of dimensions, starting from 1.8 μm and reaching

4.0 μm . However, a closer look reveals that these grains were finer than those comprising the 0.0Ag-MNPs composition. Specifically, the large grains consisted of aggregates of spherical particles with dimensions ranging from 0.15 to 0.60 μm , exhibiting also a somewhat high intergranular porosity than 0.0Ag-MNPs. The composition with the highest concentration of Ag ions, 0.2Ag-MNPs, also formed agglomerated grains with sizes ranging from 1.0 to 1.7 μm . However, as with 0.1Ag-MNPs, a closer look revealed that these grains consisted of spheres with

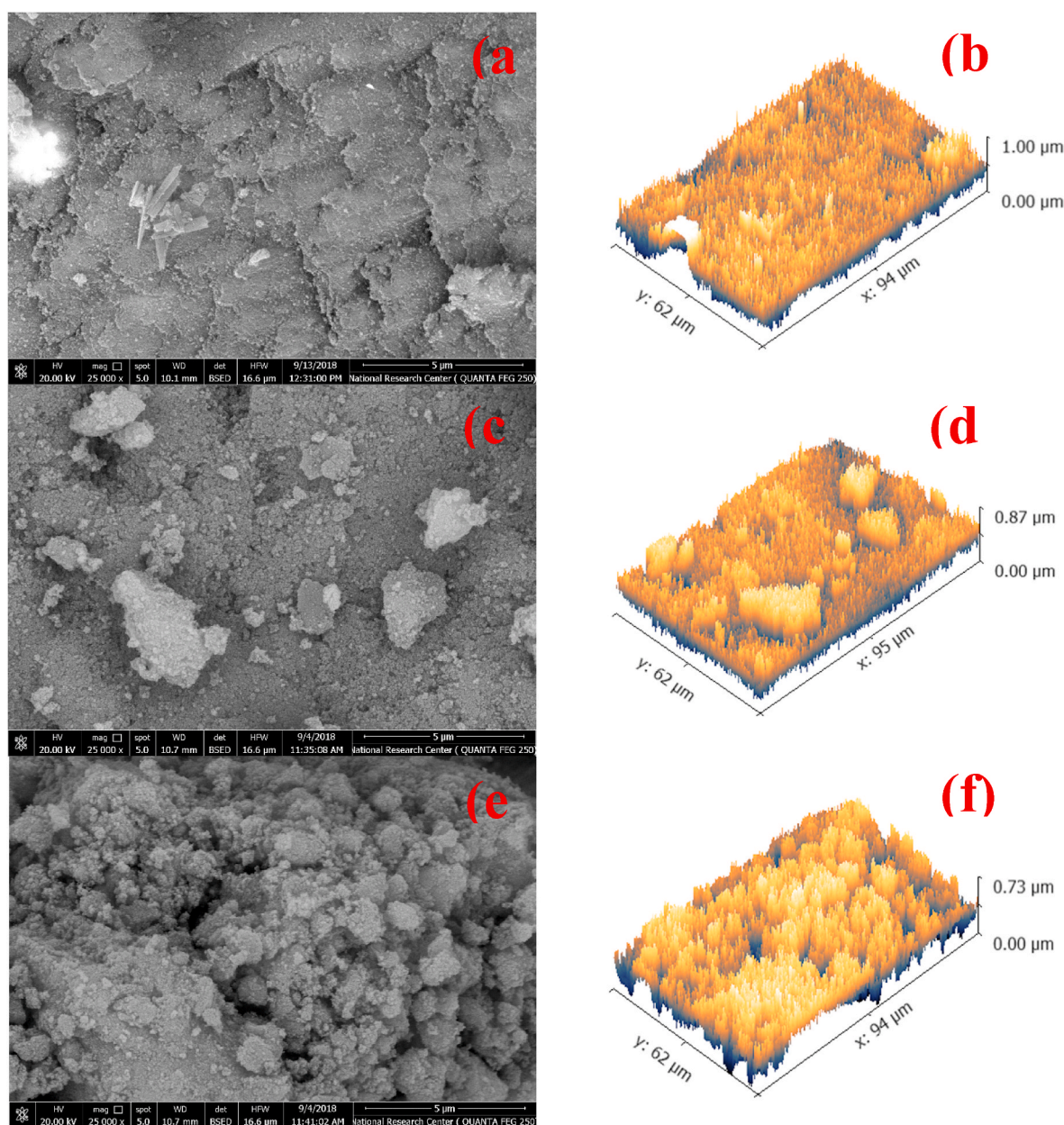


Fig. 6(a–f). FESEM micrographs showing the morphology and surface roughness profiles for Ag-MNPs with different concentrations of Ag ions: (a, b) 0.0Ag-MNPs, (c, d) 0.1Ag-MNPs and (e, f) 0.2Ag-MNPs.

diameters of 0.16–0.30 μm . Moreover, a high intergranular porosity accompanied the very rough powder surface.

The small size of the fine particles comprising the larger grains was the major contributor to the moderately high roughness of the surface detected in all the compositions. However, with the addition of Ag ions and an increase in their concentration in the material, surface roughness progressively increased. The very fine reduction of the grain size with the addition of Ag appears to be the major factor causing this increase in the surface roughness, with the intergranular porosity coming next. Specifically, the roughness average (R_a) started from 42.7 nm for pure MNPs, and then increased to 49.8 nm for 0.1Ag-MNPs and to 61.1 nm for 0.2Ag-MNPs, as reported in Table 6.

The root mean square roughness (R_q) and the maximum height of the roughness (R_t) followed the same trend as that applying to R_a . This increase in the surface roughness with an increase in the Ag dopant concentration could be explained by its causing crystallographic distortions confirmed in the XRD analysis. These distortions create large amounts of defects in the crystals, including those located on the surface (steps, kinks, ad atoms, etc.). These surface defects do not only present a source of roughness *per se*, but they also cause the further misalignment in the packing of the neighboring grains, which increases the inter-granular porosity and thus, the surface roughness [80,81]. Because of the higher surface energy associated with rougher surfaces, such material structures tend to display a higher chemical activity, in part because these defects can act as ionic traps in the host environment. As a result, the chemical activity of the material could be adjusted to the ambient environment by controlling the composition and, in turn, a micro-structural feature such as roughness.

3.7. Morphological features of nanofibrous Ag-MNPs@PCL scaffolds

The cell binding affinity and strength usually scale directly with the surface roughness of biomaterials, for which reason the inspection and the control of surface roughness are important aspects of the design of biomaterials for an optimal interface with living tissues. Fig. 7(a–f) illustrates changes in the surface morphology of PCL nanofibers with the incorporation of MNPs with different Ag contents. Without any added Ag ions, MNPs@PCL adopted the form of non-oriented nanofibers with diameters starting from 0.38 μm at their lowest and reaching 1.2 μm at their highest. This wide range of size distribution is ascribed to the branching of the fibers, where the larger fibers split into smaller ones during the extrusion process. This phenomenon may provide more robust mechanical properties to the material as the result of the greater degree of entwinement of the dispersed nanofibers. The high porosity and the low roughness could also be observed, as well as the occasional presence of MNPs decorating the nano-fiber surface (Fig. 7(a and b)).

With the addition of Ag ions at the lower of the two concentrations, no significant changes were observed in the morphology of Ag-MNPs@PCL nanofibers, as they continued to exist in the form of a networked fibrous scaffold. Two ranges of the fiber diameters were detected: 0.4–0.8 μm and 2.1–2.7 μm . Here, the thinner fibers branched from

Table 6

Surface roughness parameters as a function of the concentration of the Ag ion dopant in MNPs, including the roughness average (R_a), root mean square roughness (R_q), the maximum height of the roughness (R_t), maximum roughness valley depth (R_v), maximum roughness peak height (R_p), and the average maximum height of the roughness (R_{tm}).

Composition	R_a (nm)	R_q (nm)	R_t (nm)	R_v (nm)	R_p (nm)	R_{tm} (nm)
0.0Ag-MNPs	42.7 ± 3.4	54.4 ± 5.6	376.4 \pm 16.9	205.5 ± 5.6	170.9 ± 9.5	300.7 \pm 9.8
0.1Ag-MNPs	49.8 ± 3.7	62.5 ± 5.4	438.1 \pm 18.4	197.2 ± 8.3	240.9 ± 5.6	330.5 \pm 8.4
0.2Ag-MNPs	61.1 ± 4.6	78.4 ± 6.5	520.4 \pm 9.5	243.7 ± 5.4	276.7 ± 8.5	445.9 \pm 13.2

the larger ones, as it was the case with MNPs@PCL fibers too. Porosity appeared slightly lower and surface roughness slightly higher compared to MNPs@PCL. However, the morphology of Ag-MNPs@PCL scaffolds underwent a more significant change at the highest concentration of Ag ions in the MNP phase, i.e., 0.2Ag-MNPs@PCL. The nanofibers became visibly thinner and more branched. The porosity was even lesser than that of the compositions with lower amounts of Ag, and Ag-MNPs were even more prominent on the surface of the nanofibers. Although the majority of MNPs continued to be predominantly encapsulated by the nanofibers, a significant portion of them protruded from the surface. This effect can be explained by changes to the viscosity and conductivity of the precursor solution entailing changes in the crystallinity due to the incorporation of Ag cations, but also by changes to the Ag-MNPs/PCL interface. With more MNPs ejected to the surface of the nanofibers when the NPs are less crystalline and contain more Ag, the interface between PCL and MNPs may be more energetically favorable when the latter are more crystalline.

Changes to the surface roughness of the nanofibrous scaffolds with the addition of Ag to the MNP phase are illustrated in Fig. 8(a–c) and also shown in Table 7.

The roughness average (R_a) exhibited a slight growth with the addition of Ag, from 31.6 ± 6.5 to 32.0 ± 3.4 to 34.0 ± 4.5 nm for 0.0Ag-MNPs@PCL, 0.1Ag-MNPs@PCL and 0.2Ag-MNPs@PCL, respectively. R_q followed the trend in R_a , while R_t displays a more fluctuant response, initially decreasing from 470.9 ± 9.5 to 388.0 ± 8.4 nm with the addition of Ag to MNPs@PCL, but then recovering at the higher concentration of Ag. Moreover, the maximum roughness peak height (R_p) plunged dramatically from 325.5 ± 13.5 to 225.0 ± 14.6 nm with the transition from 0.0Ag-MNPs@PCL to 0.1Ag-MNPs@PCL and did not fully recover with the further addition of Ag. This deviation from a singular trend for all the roughness parameters can be explained by the specifics of each. Namely, while R_a represents the averages of peaks and notches, R_v describes the depths of notches only and R_p concentrates on the peaks. Knowing this, it could be inferred that 0.2Ag-MNPs@PCL shows deep notches, but not as high peaks, and it is opposite for 0.0Ag-MNPs@PCL. In any case, the roughness observed and largely promoted by the surface appearance of Ag-MNPs, particularly in the 0.2Ag-MNPs@PCL composition, could facilitate the adhesion with the host tissues through mechanical and physicochemical processes. The former imply the interlocking of the polymeric chains with the topography of the host surface, while the latter stem from bonding at the atomic scale. The higher chemical activity of the surface with a higher concentration of crystallographic defects and rougher grains, such as that of 0.2Ag-MNPs@PCL, could facilitate the integration of the dressing and enhance the effects of the therapy aimed toward the reconstruction of the skin tissue. Consequently, the healing rate could be traced to the physicochemical properties of the nano-fibrous scaffold surface, as demonstrated here, could be tailored by controlling the composition of its NP additive.

3.8. Mechanical properties of nanofibrous scaffolds

To be used in wound dressing applications, a scaffold must satisfy very specific mechanical requirements. One of them is a sufficiently high tensile strength, given that tension is the most frequent stress mode imparted on wound dressings and skin patches. The results of the examination of mechanical properties of nanofibers with different Ag contents in the MNP phase are presented in Fig. 9 and Table 8.

The tensile strength started from 4.15 ± 0.21 MPa for 0.0Ag-MNPs@PCL, but then got reduced to 3.93 ± 0.32 for 0.1Ag-MNPs@PCL, before increasing to 4.42 ± 0.25 MPa for 0.2Ag-MNPs@PCL. The elasticity of the nanofibers is another crucial parameter, and the strain at break continuously increased with the Ag addition, from $105.1 \pm 3.5\%$ for 0.0Ag-MNPs@PCL to $147.4 \pm 3.4\%$ for the composition with the highest concentration of Ag. An equally drastic improvement with the addition of Ag applied to toughness, a measure of the total required

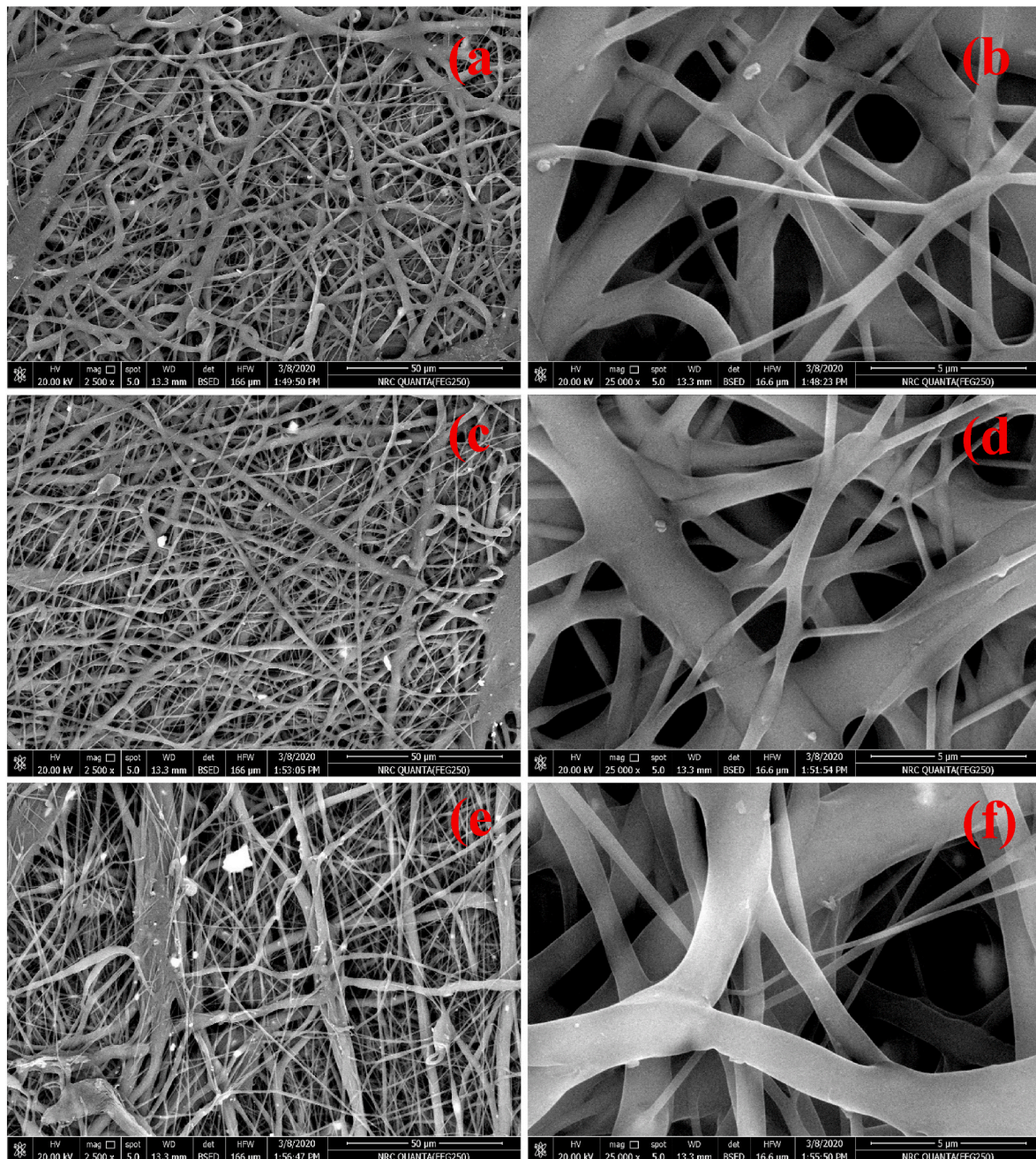


Fig. 7(a–f). FESEM micrographs of nanofibrous Ag-MNPs@PCL scaffolds with different concentrations of Ag ions: (a, b) 0.0Ag-MNPs@PCL, (c, d) 0.1Ag-MNPs@PCL, and (e, f) 0.2Ag-MNPs@PCL.

energy for scaffolds to break. It grew continuously, from 2.73 ± 0.31 to 3.60 ± 0.42 to 4.25 ± 0.33 MJ/m³ for 0.0Ag-MNPs@PCL, 0.1Ag-MNPs@PCL and 0.2Ag-MNPs@PCL, respectively. The porosity underwent a similarly constant, but far lesser increase with the addition of Ag, remaining in the 85–90% range for all the compositions, as it is reported in Table 8. These mechanical properties compare well with the similar properties of the human skin [82–84] which include the ultimate tensile strength of 15–25 MPa, the mean strain energy of 4–8 MJ/m³, and the strain at break of 130–150%.

3.9. Contact angle measurements

The hydrophobic nature of pristine PCL restricts its wide application. However, modified with the additive Ag-MNPs, the hydrophilicity of the polymer should increase, thus improving the applicability of the scaffold

as a biomaterial. Thus, as obvious from Fig. 10, the contact angle exhibited a decreasing trend, from $105.4 \pm 4.5^\circ$ to $96.3 \pm 5.2^\circ$ to $88.5 \pm 4.1^\circ$ for 0.0Ag-MNPs@PCL, 0.1Ag-MNPs@PCL and 0.2Ag-MNPs@PCL, respectively. This variation in the contact angle with the Ag content agrees well with the increased surface roughness with Ag concentration in the MNP phase (Table 7), but also with the increased hydrophilicity at higher Ag contents deduced from the FTIR analysis (Fig. 3).

3.10. HFB4 cell viability

The biocompatible response of the material with respect to the biological host environment is a vital prerequisite for its application as a biomaterial. Therefore, cultivation of the nanofibrous scaffold in the HFB4 melanocyte culture for 3 days was carried out. As seen in Fig. 11, the cell viability of the undoped composition, 0.0Ag-MNPs@PCL, was

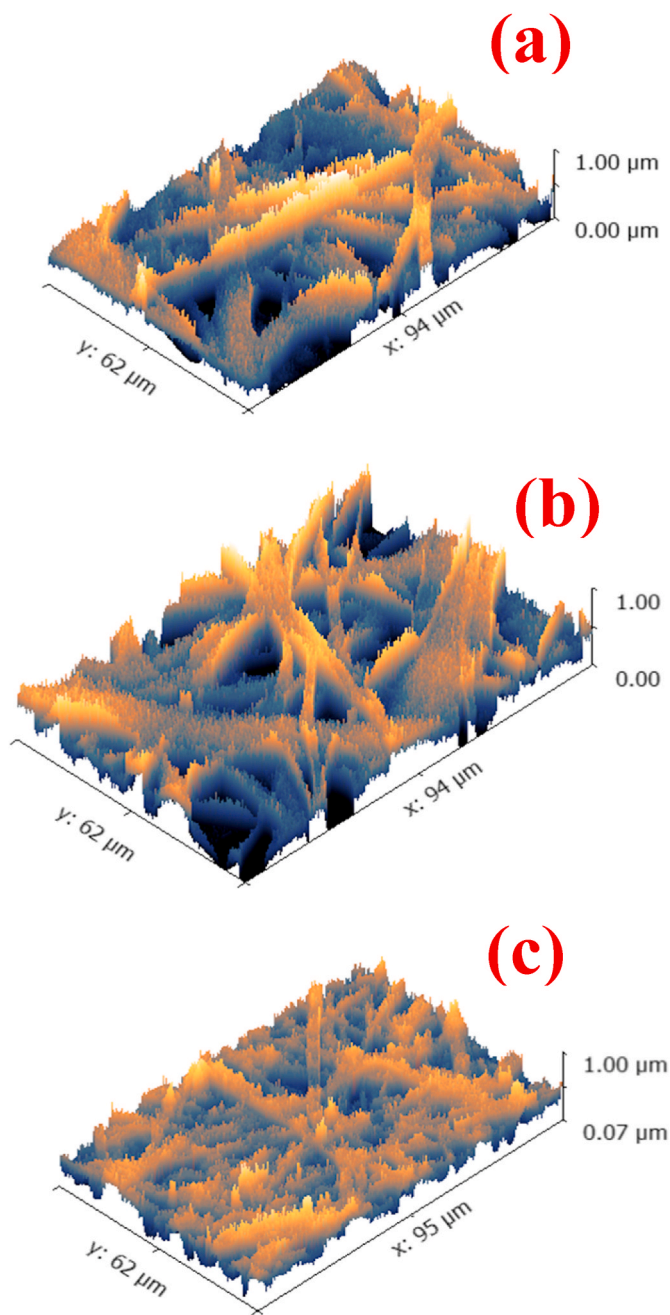


Fig. 8(a–c). Dependency of the surface roughness of Ag-MNPs@PCL scaffolds on the concentration of Ag ions: (a) 0.0Ag-MNPs@PCL, (b) 0.1Ag-MNPs@PCL and (c) 0.2Ag-MNPs@PCL.

Table 7

Surface roughness parameters as a function of the concentration of the Ag ion dopant in Ag-MNPs@PCL nanofibrous scaffolds, including (R_a), (R_q), (R_t), (R_v), (R_p), and (R_{tm}).

Composition	R_a (nm)	R_q (nm)	R_t (nm)	R_v (nm)	R_p (nm)	R_{tm} (nm)
0.0Ag-MNPs@PCL	31.6 ± 6.5	41.3 ± 3.4	470.9 ± 9.5	145.5 ± 4.5	325.5 ± 13.5	247.6 ± 9.7
0.1Ag-MNPs@PCL	32.0 ± 3.4	44.0 ± 5.4	388.0 ± 8.4	163.0 ± 9.9	225.0 ± 14.6	282.0 ± 6.8
0.2Ag-MNPs@PCL	34.0 ± 4.5	49.0 ± 3.5	467.0 ± 8.9	202.0 ± 10.5	265.0 ± 11.4	330.0 ± 11.5

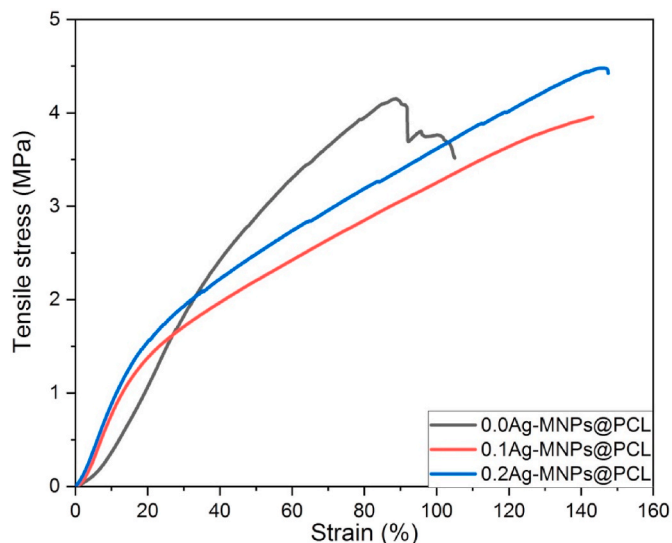


Fig. 9. Tensile stress-strain curve for nanofibrous Ag-MNPs@PCL scaffolds with different concentrations of Ag ions.

Table 8

Mechanical properties of nanofibrous Ag-MNPs@PCL scaffolds with different concentrations of Ag ions, including tensile strength, strain at break, toughness, and porosity.

Composition	Tensile strength (MPa)	Strain at break (%)	Toughness (MJ/m^3)	Porosity (%)
0.0Ag-MNPs@PCL	4.15 ± 0.21	105.1 ± 3.5	2.73 ± 0.31	84.75 ± 3.4
0.1Ag-MNPs@PCL	3.93 ± 0.32	142.5 ± 4.6	3.60 ± 0.42	85.78 ± 2.5
0.2Ag-MNPs@PCL	4.42 ± 0.25	147.4 ± 3.4	4.25 ± 0.33	87.93 ± 3.1

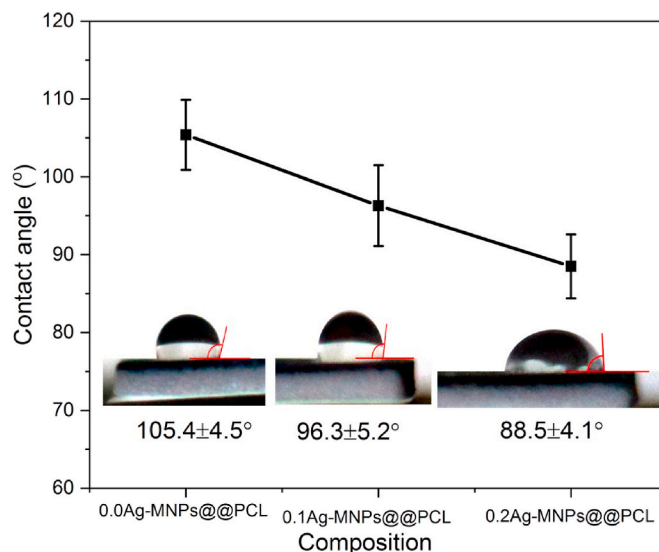


Fig. 10. Variation of the contact angle as a function of the concentration of Ag in the MNP phase of nanofibrous MNPs@PCL scaffolds.

94.1 ± 5.1% and it got enhanced to 98.4 ± 3.2% for 0.2Ag-MNPs@PCL. Exposure of mammalian cells to metallic Ag in the particulate form is known to elicit a toxic response [85], but doping materials with Ag ions mostly does not tend to cause adverse effects on similar cell lines [86, 87], presumably because of the more sustained release of Ag at lower

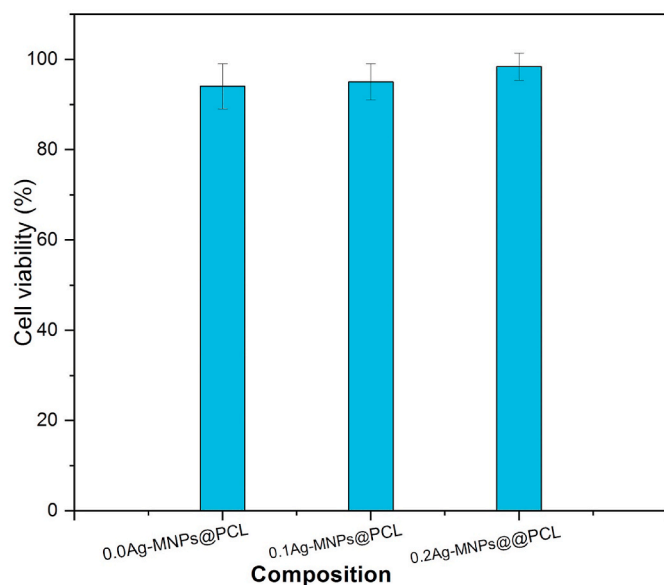


Fig. 11. Cell viability after the cultivation of the HFB4 cell line *in vitro* on nanofibrous Ag-MNPs@PCL with different concentrations of Ag ions for 3 days.

doses than those resulting from the application of Ag in the metallic form.

In this study, not only was the response of human skin melanocytes to the addition of Ag to the MNP phase of the scaffolds perfectly viable, but there was even a mild, albeit statistically insignificant ($p > 0.05$), increase in cell viability following an increase in the concentration of Ag in the MNPs component of the scaffolds. This indicates high biocompatibility of the nanofibrous scaffolds and no toxic effects of the release of constitutive ions, nanoparticles or organic oligomers into the biological media.

3.11. HFB4 cell attachment

The adhesion of HFB4 cells onto the nanofibrous scaffolds was examined after 3 days of cultivation *in vitro*. Fig. 12(a–f) illustrates the HFB4 growth on MNPs@PCL scaffolds with different concentrations of Ag ions.

Aside from the more abundant presence of particles forming as precipitates from the cell culture medium and adhering onto the scaffold; all compositions displayed prominent cell attachment. With the potential formation of bioactive calcium phosphate nanoparticles, the cell culture medium is supersaturated [88]. It cannot be excluded that their adherence onto the nanofibers presents one of the driving forces for the subsequent or simultaneous attachment of cells as well. Nevertheless, the cells adhered tightly onto the surface of all materials, with the cells forming atop the 0.1Ag-MNPs@PCL composition appearing more mature than the cells formed atop the 0.0Ag-MNPs@PCL composition. Moreover, the cells tended to be more elongated in the latter case and proliferated not only on the surface of the fibers, but also inside the deeper pores. This is a strong indicator of the vital importance of porosity not only for the facilitation of vascularization and the transport of oxygen and nutrients, but also for the basic cell growth. As far as the cell growth on 0.2Ag-MNPs@PCL composition is concerned, the cells apparently spread and proliferated across the large portions of the volume the nanofibrous scaffold, with their filopodia tending to follow the fiber curvature.

Here, it could be mentioned that the cell growth throughout the scaffold volume depends strongly on its hydrophilicity. One reason for this is that wetting precedes the protein binding and the subsequent attachment of the cells. Based on earlier reports and FT-IR results of this study, pure PCL is comparatively hydrophobic. However, the addition of

MNPs, both alone and doped with Ag ions, mitigates this extreme hydrophobic behavior of PCL and renders it more prone to cell attachment. With an increase in the concentration of the Ag dopant inside Ag-MNPs, the crystallinity of the NPs decreases, which change the interface with PCL and increases their surface presence, consequently lowering the hydrophobicity. The same effect presumably leads to an increased surface roughness, which is a topological factor favoring hydrophilicity of the surface. The adherence of proteins, for example, is said to proceed better on surfaces activated with sufficient roughness [89]. Furthermore, MNPs could provide the reservoir of ions releasable through the biological environment to provide essential elements for the fast healing process. Consequently, the modification of biomaterials with compositionally controlled nano-particulate additives proves as a viable approach in designing scaffolds for wound healing and tissue regeneration.

3.12. Antibacterial examination

Bacterial infection is one of the most common causes of delayed or failed healing of the tissue after the injury. Therefore, it is essential to endow scaffold biomaterials with antibacterial properties that prevent the bacterial infection and support the integration process. Ideally, the antibacterial species should be released gradually through the extracellular space and into the wound so as to prevent the burst release and any toxic effects associated with it. The primary reason for choosing Ag⁺ ions as dopants in MNPs was their displaying the ability to inhibit the bacterial growth and thereby prevent inflammation and facilitate wound healing. The antibacterial examination was performed against Gram-negative *E. coli* and Gram-positive *S. aureus*, and the results are shown in Fig. 13.

No inhibition zone was detected for the untreated agar plates inoculated with the bacteria (control). Adding 0.0Ag-MNPs@PCL onto the agar plate did not result in any inhibition zone either against *E. coli* or *S. aureus*. However, 0.1Ag-MNPs@PCL showed a significant antibacterial effect, with the inhibition activity of 79.2 ± 4.5 and $80.1 \pm 4.9\%$ against *E. coli* and *S. aureus*, respectively. Increasing the concentration of Ag in the material to 0.2Ag-MNPs@PCL resulted in a further increase in the inhibition activity to 87.5 ± 5.7 ($p = 0.12$ vs. 0.1Ag-MNPs@PCL) and $84.3 \pm 7.5\%$ ($p = 0.46$ vs. 0.1Ag-MNPs@PCL) for *E. coli* and *S. aureus*, respectively. This has proven that the antibacterial activity of Ag-MNPs@PCL is high and that it is solely due to the presence of Ag, with neither the elongated morphologies of PCL nanofibers nor MNPs *per se* playing any significant role in promoting this activity. The mechanism by which Ag ions inhibit the bacterial growth is not fully elucidated, but has been assigned to their ability to interact with the bacterial cell walls and generate reactive oxygen species (ROS) [90]. In addition, Ag ions have been noted for their ability to interact with the intracellular enzyme of bacteria and cause DNA damage and impair metabolism, which leads to the collapse of bacterial cells. Overall, combining both healing promotion and the antibacterial effect by a biomaterial is a positive indicator of its potential for a prospective clinical utilization.

3.13. In vivo wound healing assessment

To further assess this clinical potential of the developed Ag-MNPs@PCL films for wound healing applications, *in vivo* tests on rats were conducted. Fig. 14 shows the progress in wound healing via optical images starting from the day zero and then continuing to days 3, 7 and 10 following the treatment with nanofibrous Ag-MNPs@PCL scaffolds.

The control animals were allowed to heal without any dressing, while the wound area was measured at different times and compared with the initial wound size to determine the healing rate. Obviously, the size of the wound tended to decrease after the treatment. After ten days of treatment, the 0.2Ag-MNPs@PCL scaffolds showed the average wound healing rate of $92 \pm 3\%$, which was the highest healing rate

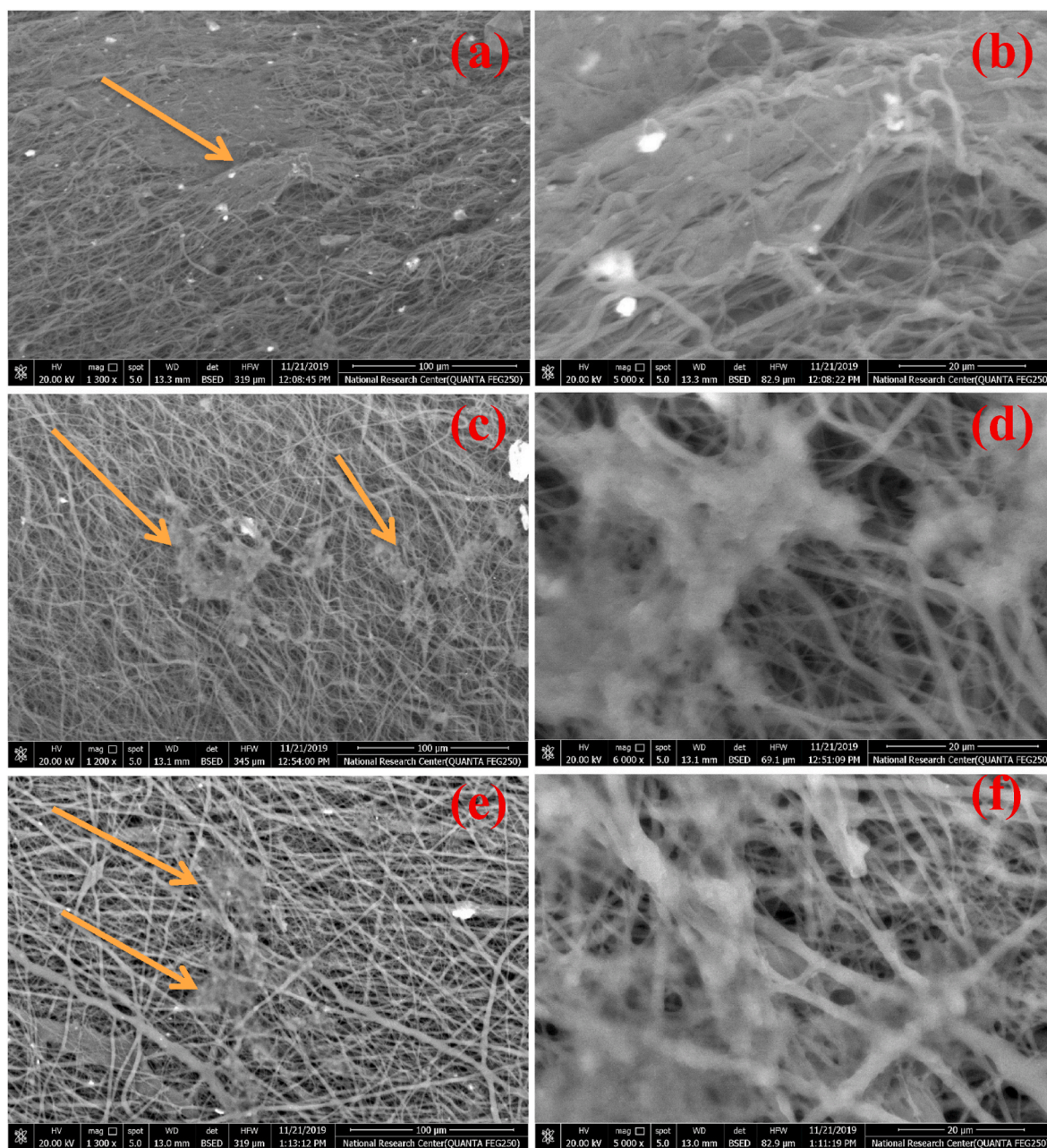


Fig. 12(a–f). FESEM micrographs showing the HBF4 cell attachment on nanofibrous Ag-MNPs@PCL scaffolds after *in vitro* cultivation for 3 days: (a, b) 0.0Ag-MNPs@PCL, (c, d) 0.1Ag-MNPs@PCL and (e, f) 0.2Ag-MNPs@PCL.

among all the sample groups. The lower concentration of Ag, 0.1Ag-MNPs@PCL, achieved the healing rate of $65 \pm 7\%$, which was higher than the healing rate of $51 \pm 4\%$ in the 0.0Ag-MNPs@PCL group. The difference in the healing rate between all the treatment groups was statistically significant ($p < 0.05$). The images of treated wounds also revealed an overall improvement in the wound appearance, with no scarring or inflamed wound edges. In contrast, the untreated wounds demonstrated miniscule healing progress during the ten days of treatment.

Fig. 15 shows photomicrographs of the healed tissues following 10 days of exposure to 0.0Ag-MNPs@PCL and 0.2Ag-MNPs@PCL scaffolds in comparison with the control group. Examination of the skin healed without any treatment showed high levels of necrosis in the hair follicles at the dermis and the atrophy in sebaceous glands. On the other hand, no histopathological alterations were detected in the epidermal and dermal layers containing the hair follicles and the sebaceous glands in animals

treated with the nanofibrous scaffolds.

This excellent wound healing achieved with the application of the scaffolds could be partly attributed to the biocompatibility of the electrospun nanofibrous PCL scaffolds *per se*, but also to the antibacterial activity of Ag ions. Obviously, they provide the material with a considerable antibacterial activity, but they do not cause any toxicity to the mammalian cells or tissues. The presence of MNPs may be a crucial wound healing factor not only in terms of their providing the reservoir for the Ag ions, but also through increasing the hydrophilicity and the surface roughness and accelerating the coagulation. Rapid coagulation prevents excessive bleeding and promotes quick closure of the wound, thus minimizing the chances of its contracting bacterial contaminants.

4. Summary

Magnetite nanoparticles doped with different concentrations of Ag

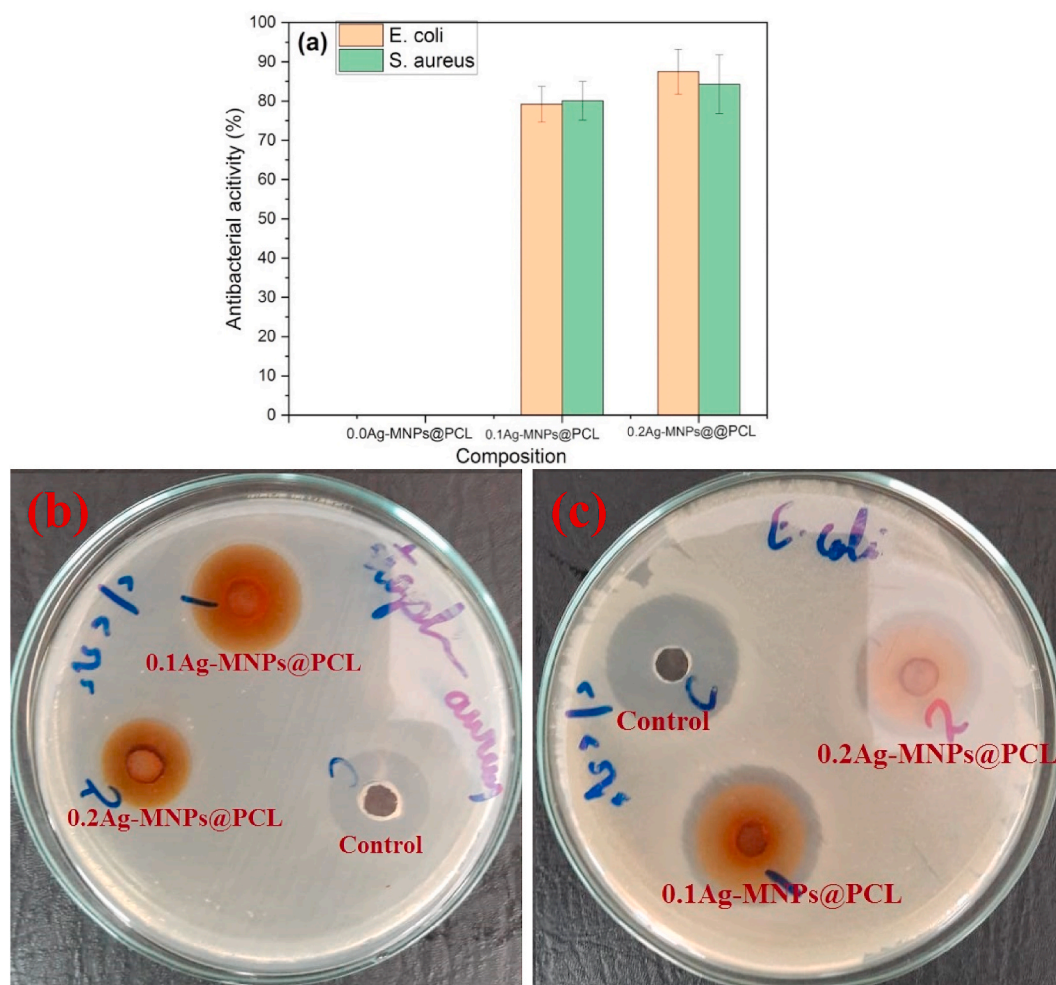


Fig. 13. Antibacterial behavior of nanofibrous Ag-MNPs@PCL scaffolds with different concentrations of the Ag ion against *E. coli* and *S. aureus* after 3 days of exposure, including the representative agar plates for (b) *S. aureus* and (c) *E. coli*.

ions were synthesized using co-precipitation and embedded inside nanofibrous PCL scaffolds produced using electrospinning. This composite material and its magnetite component were characterized in detail for their microstructure, crystal structure, phonon spectra, surface composition and magnetic properties. Combined photoelectron spectroscopic and diffractometric studies demonstrated that Ag was incorporated in the magnetite lattice in form of cations, without forming any metallic clusters. The accommodation of Ag ions expanded the unit cell and lowered the crystallinity of the magnetite phase, which increased the concentration of topological irregularities and inhibited agglomeration. Specifically, the Rietveld analysis of Ag-doped magnetite indicated that crystallinity decreased from 26.3 to 9.4 nm and the lattice parameter a expanded from 8.355 to 8.364 Å with the transition from pure magnetite (0.0Ag-MNPs) to magnetite with the highest concentration of Ag ions (0.2Ag-MNPs). Morphological investigations showed that the average size of nanoparticle agglomerates decreased with the addition of Ag due to induced crystallographic disorder, while R_a and R_p as the measures of the surface roughness increased from 42.7 to 170.9 nm for 0.0Ag-MNPs to 61.1 and 276.7 nm for 0.2Ag-MNPs. The XPS analysis confirmed the amorphization of the surface due to the addition of Ag ions, which was accompanied by a broadened distribution of Fe–O coordination numbers and types. The magnetic characterization demonstrated a significant decrease in saturation magnetization, from over 100 emu/g for 0.0Ag-MNPs to 32.3 emu/g for 0.2Ag-MNPs. With the help of the XPS analysis, this effect was shown to be due to the preferential accommodation of Ag ions at the tetrahedral sites of the

spinel lattice and the resulting reduction of the concentration of Fe^{2+} ions at the octahedral sites, leading to diminished double exchange interaction.

The nanofibrous scaffolds exhibited a greater surface protrusion of the nanoparticles at higher Ag concentrations, as the result of which their surface roughness and porosity all tended to increase with the addition of the highest concentration of Ag to the magnetite phase. The composite materials were also assessed for their potential as wound dressings *in vitro* and *in vivo*. Cell viability examination against a human skin melanocytes showed that all the compositions were highly biocompatible, with viabilities increasing with the concentration of Ag ions in their magnetite phase. The antibacterial activity against Gram-negative *E. coli* and Gram-positive *S. aureus* was none for the Ag-free scaffolds and it increased with the concentration of Ag ions in the magnetite phase, being exceptional already at its lowest concentration. *In vivo* examination of wound healing demonstrated that the healing rate was miniscule in the control group, but got enhanced to over 50% for the scaffold with no Ag ions in the magnetite phase and to over 90% for the scaffold with the highest concentration of Ag ions. Atrophy of sebaceous glands and the necrosis of hair follicles were evident in the control animals, but no abnormalities were detected in the epidermal and dermal layers of animals whose wounds were treated with the scaffolds supplemented with Ag-doped magnetite nanoparticles. These results imply an excellent potential of the composite nanofibrous scaffolds for use as wound dressings and in other reconstructive skin therapies. Further development of such constructs would benefit the current clinical needs

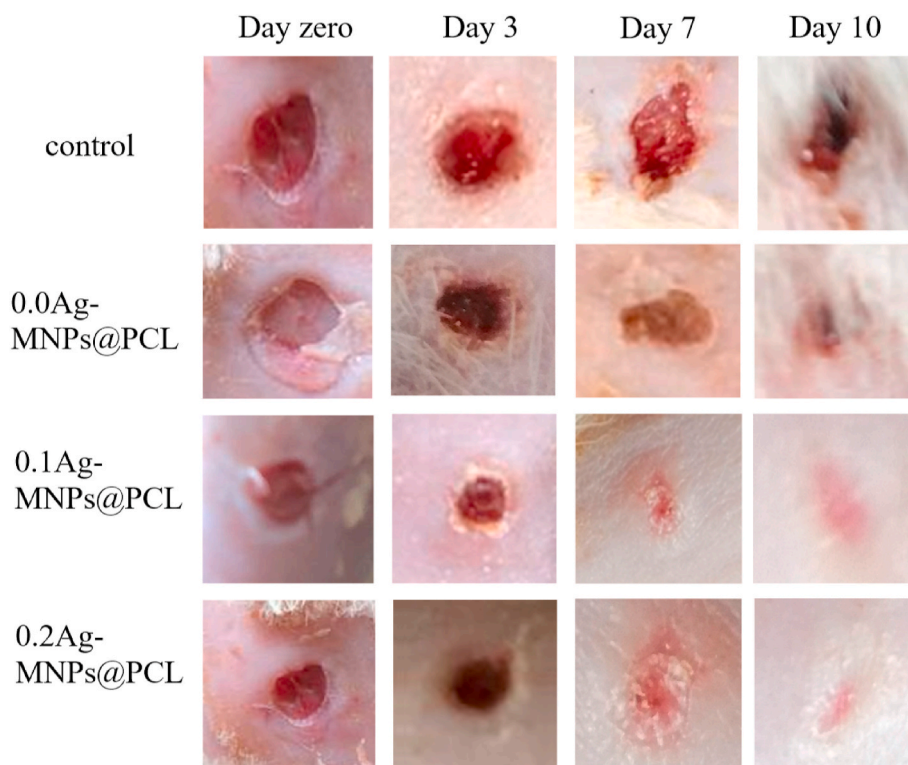


Fig. 14. Representative optical images of rat skin wound healing for Ag-MNPs@PCL nanofibrous scaffolds with different concentrations of the Ag ion after 0, 3, 7 and 10 days of treatment.

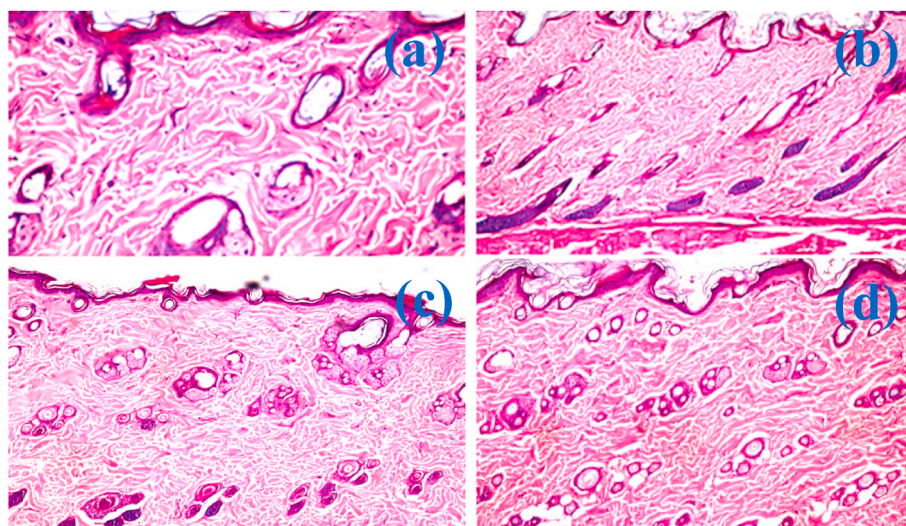


Fig. 15. Photomicrographs at 60 \times (a) and 40 \times (b–d) magnification of untreated rat skin showing the atrophy of sebaceous glands (a) as well as the necrosis of hair follicles (b). Photomicrographs of treated rat skin with 0.0Ag-MNPs@PCL (c) and 0.2Ag-MNPs@PCL (d), showing normal histological structure of the epidermis and the underlying dermal layer with the sebaceous glands and hair follicles.

for wound dressings that simultaneously inhibit the bacterial growth and promote tissue regeneration.

CRediT authorship contribution statement

M.K. Ahmed: Conceptualization, Methodology, Formal analysis, Data curation, Investigation, Visualization, Resources, Writing - original draft. **M.A. Zayed:** Investigation, Data curation, Visualization. **S.I. El-dek:** Conceptualization, Investigation, Visualization. **Mayssa Abdel Hady:** Investigation, Resources. **Doaa H. El Sherbiny:** Investigation.

Vuk Uskoković: Conceptualization, Formal analysis, Validation, Visualization, Writing - original draft, Writing - review & editing.

Declaration of competing interest

The authors declare that they have no known competing financial interests or personal relationships that could have appeared to influence the work reported in this paper.

Acknowledgement

This work has been acknowledged by Cairo University.

References

- [1] G. Rivero, M. Meuter, A. Pepe, M.G. Guevara, A.R. Boccaccini, G.A. Abraham, Nanofibrous membranes as smart wound dressings that release antibiotics when an injury is infected, *Colloid. Surface. Physicochem. Eng. Aspect.* 587 (2020), 124313.
- [2] S. Homaeigohar, A.R. Boccaccini, Antibacterial biohybrid nanofibers for wound dressings, *Acta Biomater.* 107 (2020) 25–49.
- [3] M. Rahimi, E.B. Noruzi, E. Sheykhsaran, B. Ebadi, Z. Kariminezhad, M. Molapour, et al., Carbohydrate polymer-based silver nanocomposites: recent progress in the antimicrobial wound dressings, *Carbohydr. Polym.* 231 (2020), 115696.
- [4] F. Liu, X. Li, L. Wang, X. Yan, D. Ma, Z. Liu, et al., Sesamol incorporated cellulose acetate-zinc composite nanofiber membrane: an efficient strategy to accelerate diabetic wound healing, *Int. J. Biol. Macromol.* 149 (2020) 627–638.
- [5] E. Esmaili, T. Eslami-Arshaghi, S. Hosseinzadeh, E. Elahirad, Z. Jamalpoor, S. Hatamie, et al., The biomedical potential of cellulose acetate/polyurethane nanofibrous mats containing reduced graphene oxide/silver nanocomposites and curcumin: antimicrobial performance and cutaneous wound healing, *Int. J. Biol. Macromol.* 152 (2020) 418–427.
- [6] M. Najafiasl, S. Osfouri, R. Azin, S. Zaeri, Alginate-based electrospun core/shell nanofibers containing dextran: a good candidate for wound dressing, *J. Drug Deliv. Sci. Technol.* 57 (2020), 101708.
- [7] A. Das, R. Uppaluri, C. Das, Compositional synergy of poly-vinyl alcohol, starch, glycerol and citric acid concentrations during wound dressing films fabrication, *Int. J. Biol. Macromol.* 146 (2020) 70–79.
- [8] K. Chen, F. Wang, S. Liu, X. Wu, L. Xu, D. Zhang, In situ reduction of silver nanoparticles by sodium alginate to obtain silver-loaded composite wound dressing with enhanced mechanical and antimicrobial property, *Int. J. Biol. Macromol.* 148 (2020) 501–509.
- [9] H.R. Bakhsheshi-Rad, A.F. Ismail, M. Aziz, M. Akbari, Z. Hadisi, M. Omid, et al., Development of the PVA/CS nanofibers containing silk protein sericin as a wound dressing: in vitro and in vivo assessment, *Int. J. Biol. Macromol.* 149 (2020) 513–521.
- [10] S. Baek, H. Park, M. Kim, D. Lee, Preparation of PCL/(+)-catechin/gelatin film for wound healing using air-jet spinning, *Appl. Surf. Sci.* 509 (2020), 145033.
- [11] R. Augustine, S.R.U. Rehman, R. Ahmed, A.A. Zahid, M. Sharifi, M. Falahati, et al., Electrospun chitosan membranes containing bioactive and therapeutic agents for enhanced wound healing, *Int. J. Biol. Macromol.* 156 (2020) 153–170.
- [12] M.K. Ahmed, S.F. Mansour, R. Al-Wafi, Nanofibrous scaffolds of epsilon-polycaprolactone containing Sr/Se-hydroxyapatite/graphene oxide for tissue engineering applications, *Biomed. Mater.* (2020), <https://doi.org/10.1088/1748-605X/ab7ff5>. In press.
- [13] M.K. Ahmed, R. Al-Wafi, S.F. Mansour, S.I. El-dek, V. Uskoković, Physical and biological changes associated with the doping of carbonated hydroxyapatite/polycaprolactone core-shell nanofibers dually, with rubidium and selenium, *Journal of Materials Research and Technology* 9 (2020) 3710–3723.
- [14] M.K. Ahmed, R. Ramadan, S.I. El-dek, V. Uskoković, Complex relationship between alumina and selenium-doped carbonated hydroxyapatite as the ceramic additives to electrospun polycaprolactone scaffolds for tissue engineering applications, *J. Alloys Compd.* 801 (2019) 70–81.
- [15] M.K. Ahmed, S.F. Mansour, R. Al-Wafi, S.I. El-dek, V. Uskoković, Tuning the mechanical, microstructural, and cell adhesion properties of electrospun ϵ -polycaprolactone microfibers by doping selenium-containing carbonated hydroxyapatite as a reinforcing agent with magnesium ions, *J. Mater. Sci.* 54 (2019) 14524–14544.
- [16] M.K. Ahmed, A.A. Menazea, A.M. Abdelghany, Blend biopolymeric nanofibrous scaffolds of cellulose acetate/epsilon-polycaprolactone containing metallic nanoparticles prepared by laser ablation for wound disinfection applications, *Int. J. Biol. Macromol.* 155 (2020) 636–644.
- [17] W. Wentao, Z. Tao, S. Bulei, Z. Tongchang, Z. Qicheng, W. Fan, et al., Functionalization of polyvinyl alcohol composite film wrapped in a-ZnO@CuO@Au nanoparticles for antibacterial application and wound healing, *Applied Materials Today* 17 (2019) 36–44.
- [18] V. Uskoković, Entering the era of nanoscience: time to Be so small, *Biomed Nanotechnol* 9 (2013) 29.
- [19] P.Y. Hu, Y.T. Zhao, J. Zhang, S.X. Yu, J.S. Yan, X.X. Wang, et al., In situ melt electrospun polycaprolactone/Fe₃O₄ nanofibers for magnetic hyperthermia, *Materials science & engineering C, Materials for biological applications* 110 (2020), 110708.
- [20] D. Hao, G. Zhang, Y. Gong, Z. Ma, Development and biological evaluation of cerium oxide loaded polycaprolactone dressing on cutaneous wound healing in nursing care, *Mater. Lett.* 265 (2020), 127401.
- [21] R. Al-Wafi, S.F. Mansour, M.K. Ahmed, Mechanical, microstructural properties and cell adhesion of Sr/Se-hydroxyapatite/graphene/polycaprolactone nanofibers, *J. Thermoplast. Compos. Mater.* (2020), 89270572091278.
- [22] S.M. Khoshfetrat, M.A. Mehrgardi, Amplified detection of leukemia cancer cells using an aptamer-conjugated gold-coated magnetic nanoparticles on a nitrogen-doped graphene modified electrode, *Bioelectrochemistry* 114 (2017) 24–32.
- [23] J.V. Nuzhina, A.A. Shtil, A.Y. Prilepskiy, V.V. Vinogradov, Preclinical evaluation and clinical translation of magnetite-based nanomedicines, *J. Drug Deliv. Sci. Technol.* 54 (2019), 101282.
- [24] H.E. Rizk, N.E. El-Hefny, Synthesis and characterization of magnetite nanoparticles from polyol medium for sorption and selective separation of Pd(II) from aqueous solution, *J. Alloys Compd.* 812 (2020), 152041.
- [25] O. Ziv-Polat, M. Topaz, T. Brosh, S. Margel, Enhancement of incisional wound healing by thrombin conjugated iron oxide nanoparticles, *Biomaterials* 31 (2010) 741–747.
- [26] A. Moradi, Y. Kheirollahkhani, P. Fatahi, M.A. Abdollahifar, A. Amini, P. Naserzadeh, et al., An improvement in acute wound healing in mice by the combined application of photobiomodulation and curcumin-loaded iron particles, *Laser Med. Sci.* 34 (2019) 779–791.
- [27] F.I. El-Dib, D.E. Mohamed, O.A.A. El-Shamy, M.R. Mishrif, Study the adsorption properties of magnetite nanoparticles in the presence of different synthesized surfactants for heavy metal ions removal, *Egyptian Journal of Petroleum* 29 (2020) 1–7.
- [28] F. Morales, G. Márquez, V. Sagredo, T.E. Torres, J.C. Denardin, Structural and magnetic properties of silica-coated magnetite nanoaggregates, *Phys. B Condens. Matter* 572 (2019) 214–219.
- [29] J.-H. Guo, C.-B. Leng, X.-C. Zhang, T. Zafar, W. Terry Chen, W. Zhang, et al., Textural and chemical variations of magnetite from porphyry Cu-Au and Cu skarn deposits in the Zhongdian region, northwestern Yunnan, SW China, *Ore Geol. Rev.* (2019), 103245.
- [30] N. Singh, G.J. Jenkins, R. Asadi, S.H. Doak, Potential toxicity of superparamagnetic iron oxide nanoparticles (SPION), *Nano Rev.* 1 (2010).
- [31] J.C. Park, S. Yeo, M. Kim, G.T. Lee, J.H. Seo, Synthesis and characterization of novel lanthanide-doped magnetite@Au core@shell nanoparticles, *Mater. Lett.* 181 (2016) 272–277.
- [32] M.A. Zakria, A.A. Menazea, A.M. Mostafa, E.A. Al-Ashkar, Ultra-thin silver nanoparticles film prepared via pulsed laser deposition: synthesis, characterization, and its catalytic activity on reduction of 4-nitrophenol, *Surfaces and Interfaces* (2020), 100438.
- [33] L. Xu, X. Shi, Q. Qian, X. Bai, L. Xu, Q. Wang, Hydrothermal sterilization in silver nitrate solution endows plasma sprayed hydroxyapatite coating with antibacterial property, *Mater. Lett.* 263 (2020), 127258.
- [34] Q. Zhou, T. Wang, C. Wang, Z. Wang, Y. Yang, P. Li, et al., Synthesis and characterization of silver nanoparticles-doped hydroxyapatite/alginate microparticles with promising cytocompatibility and antibacterial properties, *Colloid. Surface. Physicochem. Eng. Aspect.* 585 (2020), 124081.
- [35] P. Zhou, L. Zhang, Y. Dai, W. Wu, X. Sui, Y. Zhong, et al., Construction of a metallic silver nanoparticle-decorated bismuth oxybromide-based composite material as a readily recyclable photocatalyst, *J. Clean. Prod.* 246 (2020), 119007.
- [36] M.H. Teaima, M.K. Elsayly, S.A. Omar, M.A. El-Nabarawi, K.R. Shoueir, Eco-friendly synthesis of functionalized chitosan-based nanoantibiotic system for potential delivery of linezolid as antimicrobial agents, *Saudi Pharmaceut. J.* 28 (2020) 859–868.
- [37] N.Z. Shaban, A.M. Abolsaad, K.R. Shoueir, S.A. Abdulmalek, D. Awad, S. Y. Shaban, et al., Chitosan-based dithiophenolato nanoparticles: preparation, mechanistic information of DNA binding, antibacterial and cytotoxic activities, *J. Mol. Liq.* 318 (2020), 114252.
- [38] M.T. Elsayed, A.A. Hassan, S.A. Abdelaal, M.M. Taher, M.K. Ahmed, K.R. Shoueir, Morphological, antibacterial, and cell attachment of cellulose acetate nanofibers containing modified hydroxyapatite for wound healing utilizations, *Journal of Materials Research and Technology* 9 (2020) 13927–13936.
- [39] M.F. Abdelbar, R.S. Shams, O.M. Morsy, M.A. Hady, K. Shoueir, R. Abdelmonem, Highly ordered functionalized mesoporous silicate nanoparticles reinforced poly (lactic acid) gatekeeper surface for infection treatment, *Int. J. Biol. Macromol.* 156 (2020) 858–868.
- [40] K. Shoueir, M.K. Ahmed, S.A. Abdel Gaber, M. El-Kemary, Thallium and selenite doped carbonated hydroxyapatite: microstructural features and anticancer activity assessment against human lung carcinoma, *Ceram. Int.* 46 (2020) 5201–5212.
- [41] S.F. Mansour, S.I. El-dek, M. Ismail, M.K. Ahmed, Structure and cell viability of Pd substituted hydroxyapatite nano particles, *Biomedical Physics & Engineering Express* 4 (2018), 045008.
- [42] M.K. Ahmed, S.F. Mansour, M.S. Mostafa, R. Darwesh, S.I. El-dek, Structural, mechanical and thermal features of Bi and Sr co-substituted hydroxyapatite, *J. Mater. Sci.* 54 (2018) 1977–1991.
- [43] S.F. Mansour, S.I. El-dek, M.K. Ahmed, Tailoring the structure of biphasic calcium phosphate via synthesis procedure, *Mater. Res. Express* 4 (2017), 125015.
- [44] S.F. Mansour, S.I. El-Dek, M.K. Ahmed, Physico-mechanical and morphological features of zirconia substituted hydroxyapatite nano crystals, *Sci. Rep.* 7 (2017) 43202.
- [45] R. Ramadan, Preparation, characterization and application of Ni-doped magnetite, *Appl. Phys. A* 125 (2019).
- [46] R. Ramadan, Physical study of cobalt ferrite and its application in purification of water, *Appl. Phys. A* 125 (2019).
- [47] J. Chen, D. Lu, W. Liu, J. Fan, D. Jiang, L. Yi, et al., Stability study and optimization design of small-spacing two-well (SSTW) salt caverns for natural gas storages, *Journal of Energy Storage* 27 (2020), 101131.
- [48] S.F. Mansour, S.I. El-dek, S.V. Dorozhkin, M.K. Ahmed, Physico-mechanical properties of Mg and Ag doped hydroxyapatite/chitosan biocomposites, *New J. Chem.* 41 (2017) 13773–13783.
- [49] A.M. Predescu, E. Matei, A.C. Berbecaru, C. Pantilimon, C. Dragan, R. Vidu, et al., Synthesis and characterization of dextran-coated iron oxide nanoparticles, *Royal Society open science* 5 (2018), 171525.
- [50] A.N. Kursunlu, M. Ozmen, E. Guler, Novel magnetite nanoparticle based on BODIPY as fluorescent hybrid material for Ag(I) detection in aqueous medium, *Talanta* 153 (2016) 191–196.

- [51] N.H. Abdullah, K. Shamei, M. Etesami, E. Chan Abdullah, L.C. Abdullah, Facile and green preparation of magnetite/zeolite nanocomposites for energy application in a single-step procedure, *J. Alloys Compd.* 719 (2017) 218–226.
- [52] X. An, D. Cheng, L. Dai, B. Wang, H.J. Ocampo, J. Nasrallah, et al., Synthesis of nano-fibrillated cellulose/magnetite/titanium dioxide (NFC@Fe₃O₄@TNP) nanocomposites and their application in the photocatalytic hydrogen generation, *Appl. Catal. B Environ.* 206 (2017) 53–64.
- [53] N.H. Abdullah, K. Shamei, E.C. Abdullah, L.C. Abdullah, A facile and green synthetic approach toward fabrication of starch-stabilized magnetite nanoparticles, *Chin. Chem. Lett.* 28 (2017) 1590–1596.
- [54] R. Safaei javan, M. Soleimani, A. Divsalar, A. Eidi, A. Ardeshirylajimi, Biological behavior study of gelatin coated PCL nanofibrous electrospun scaffolds using fibroblasts, *J. Paramed. Sci.* 5 (2013).
- [55] N. Gökalp, C. Ulker, Y. Guvenilir, Synthesis of polycaprolactone via ring opening polymerization catalyzed by *Candida Antarctica* lipase B immobilized onto an amorphous silica support, *J. Polym. Mater.* 33 (2016) 87–100.
- [56] N. Gökalp, C. Ulker, Y. Guvenilir, Enzymatic ring opening polymerization of ϵ -caprolactone by using A novel immobilized biocatalyst, *Advanced Materials Letters* 7 (2016) 144–149.
- [57] S.F. Mansour, R. Al-Wafi, M.K. Ahmed, S. Wageh, Microstructural, morphological behavior and removal of Cr(VI) and Se(IV) from aqueous solutions by magnetite nanoparticles/PVA and cellulose acetate nanofibers, *Appl. Phys. A* 126 (2020).
- [58] A.A. Menazea, M.K. Ahmed, Silver and copper oxide nanoparticles-decorated graphene oxide via pulsed laser ablation technique: preparation, characterization, and photoactivated antibacterial activity, *Nano-Structures & Nano-Objects* 22 (2020), 100464.
- [59] A.A. Menazea, S.A. Abdelbadie, M.K. Ahmed, Manipulation of AgNPs coated on selenium/carbonated hydroxyapatite/ ϵ -polycaprolactone nano-fibrous via pulsed laser deposition for wound healing applications, *Appl. Surf. Sci.* 508 (2020), 145299.
- [60] A.A. Menazea, M.M. Eid, M.K. Ahmed, Synthesis, characterization, and evaluation of antimicrobial activity of novel Chitosan/Tigecycline composite, *Int. J. Biol. Macromol.* 147 (2020) 194–199.
- [61] A.A. Menazea, M.K. Ahmed, Wound healing activity of Chitosan/Polyvinyl Alcohol embedded by gold nanoparticles prepared by nanosecond laser ablation, *J. Mol. Struct.* (2020), 128401.
- [62] A.A. Menazea, M.K. Ahmed, Nanosecond laser ablation assisted the enhancement of antibacterial activity of copper oxide nano particles embedded through Polyethylene Oxide/Polyvinyl pyrrolidone blend matrix, *Radiat. Phys. Chem.* 174 (2020), 108911.
- [63] W. Cai, F. Fu, L. Zhu, B. Tang, Simultaneous removal of chromium(VI) and phosphate from water using easily separable magnetite/pyrite nanocomposite, *J. Alloys Compd.* 803 (2019) 118–125.
- [64] G. Cai, X. Zhu, K. Li, X. Qi, Y. Wei, H. Wang, et al., Self-enhanced and efficient removal of arsenic from waste acid using magnetite as an in situ iron donor, *Water Res.* 157 (2019) 269–280.
- [65] S.I. El-dek, S.F. Mansour, M.A. Ahmed, M.K. Ahmed, Microstructural features of flower like Fe brushite, *Prog. Nat. Sci.: Materials International* 27 (2017) 520–526.
- [66] G. Bharath, K. Rambabu, A. Hai, S. Anwer, F. Banat, N. Ponpandian, Synthesis of one-dimensional magnetite hydroxyapatite nanorods on reduced graphene oxide sheets for selective separation and controlled delivery of hemoglobin, *Appl. Surf. Sci.* 501 (2020), 144215.
- [67] Z. Lv, S. Yang, L. Chen, A. Alsaedi, T. Hayat, C. Chen, Nanoscale zero-valent iron/magnetite carbon composites for highly efficient immobilization of U(VI), *J. Environ. Sci.* 76 (2019) 377–387.
- [68] R. D'Angelo, M. Roy, T. Pauporté, S. Delaunay, D. You, C. Mansour, et al., Study of the effect of polyacrylic acid dispersant on magnetite deposits in steam generators conditions, *Mater. Chem. Phys.* 226 (2019) 118–128.
- [69] K. Wu, D. Liu, W. Lu, K. Zhang, One-pot sonochemical synthesis of magnetite@reduced graphene oxide nanocomposite for high performance Li ion storage, *Ultrason. Sonochem.* 45 (2018) 167–172.
- [70] V.A. Svetlichnyi, A.V. Shabalina, I.N. Lapin, D.A. Goncharova, T.S. Kharlamova, A. I. Stadnichenko, Comparative study of magnetite nanoparticles obtained by pulsed laser ablation in water and air, *Appl. Surf. Sci.* 467–468 (2019) 402–410.
- [71] S. Khoei, M. Soleymani, Janus arrangement of smart polymer on magnetite nanoparticles through solvent evaporation from emulsion droplets, *Appl. Surf. Sci.* 494 (2019) 805–816.
- [72] M. Zhu, X. Li, L. Ge, Y. Zi, M. Qi, Y. Li, et al., Green synthesis of kappa-carrageenan@Ag submicron-particles with high aqueous stability, robust antibacterial activity and low cytotoxicity, *Materials science & engineering C, Materials for biological applications* 106 (2020), 110185.
- [73] T.S. Rad, A. Khataee, S. Rahim Pouran, Synergistic enhancement in photocatalytic performance of Ce (IV) and Cr (III) co-substituted magnetite nanoparticles loaded on reduced graphene oxide sheets, *J. Colloid Interface Sci.* 528 (2018) 248–262.
- [74] L. Gao, Z. Liu, Z. Yang, L. Cao, C. Feng, M. Chu, et al., Synthesis and magnetism property of manganese ferrite MnFe₂O₄ by selective reduction and oxidization roasting process, *Appl. Surf. Sci.* (2020), 145292.
- [75] R. Ghasemi, J. Echeverría, J.I. Pérez-Landazábal, J.J. Beato-Lopez, M. Naseri, C. Gómez-Polo, Effect of Cu substitution on the magnetic and magnetic induction heating response of CdFe₂O₄ spinel ferrite, *J. Magn. Magn. Mater.* 499 (2020), 166201.
- [76] T. Kaewmanee, A. Phuruangrat, T. Thongtem, S. Thongtem, Solvothermal synthesis of Mn–Zn Ferrite(core)/SiO₂(shell)/BiOBr_{0.5}Cl_{0.5} nanocomposites used for adsorption and photocatalysis combination, *Ceram. Int.* 46 (2020) 3655–3662.
- [77] M. Kamran, M. Anis-ur-Rehman, Enhanced transport properties in Ce doped cobalt ferrites nanoparticles for resistive RAM applications, *J. Alloys Compd.* 822 (2020), 153583.
- [78] V.V. Karansky, A.S. Klimov, S.V. Smirnov, Structural transformations in Mn–Zn ferrite under low-energy electron beam treatment, *Vacuum* 173 (2020), 109115.
- [79] M.M. Arman, S.I. El-Dek, Room temperature exchange bias in multifunctional Sb₂FeO₆ multiferroic, *J. Supercond. Nov. Magnetism* 30 (2016) 1221–1229.
- [80] M.K. Ahmed, S.F. Mansour, R. Ramadan, M. Afifi, M.S. Mostafa, S.I. El-dek, et al., Tuning the composition of new brushite/vivanite mixed systems for superior heavy metal removal efficiency from contaminated waters, *Journal of Water Process Engineering* 34 (2020), 101090.
- [81] M.K. Ahmed, S.F. Mansour, R. Al-Wafi, M. Afifi, V. Uskokovic, Gold as a dopant in selenium-containing carbonated hydroxyapatite fillers of nanofibrous epsilon-polycaprolactone scaffolds for tissue engineering, *Int. J. Pharm.* 577 (2020), 118950.
- [82] A.J.N.A. Gallagher, Aisling, Karine Bruyère, et al., Dynamic Tensile Properties of Human Skin, IRCOBI Conference 2012. Dublin (Ireland): International Research Council on the Biomechanics of Injury, 2012.
- [83] M. Ottenio, D. Tran, A. Ni Annaidh, M.D. Gilchrist, K. Bruyere, Strain rate and anisotropy effects on the tensile failure characteristics of human skin, *Journal of the mechanical behavior of biomedical materials* 41 (2015) 241–250.
- [84] H. Joodaki, M.B. Panzer, Skin mechanical properties and modeling: a review, *Proc. IME H J. Eng. Med.* 232 (2018) 323–343.
- [85] M. Koji Kawata, Satoshikabe in vitro toxicity of silver nanoparticles at noncytotoxic doses to HepG2 human hepatoma cells, *Environ. Sci. Technol.* 43 (2009) 5.
- [86] F. Afghah, M. Ullah, J. Seyyed Monfared Zanjani, P. Akkus Sut, O. Sen, M. Emanet, et al., 3D printing of silver-doped polycaprolactone-poly(propylene succinate) composite scaffolds for skin tissue engineering, *Biomed. Mater.* 15 (2020), 35015.
- [87] U. Lohbauer, G. Jell, P. Saravanapavan, J.R. Jones, L.L. Hench, Indirect cytotoxicity evaluation of silver doped bioglass Ag-S70C30 on human primary keratinocytes, *Key Eng. Mater.* 284–286 (2005) 431–434.
- [88] V.M. Wu, V. Uskokovic, Is there a relationship between solubility and resorbability of different calcium phosphate phases in vitro? *Biochim. Biophys. Acta* 1860 (2016) 2157–2168.
- [89] J. Ge, F. Wang, Z. Xu, X. Shen, C. Gao, D. Wang, et al., Influences of niobium pentoxide on roughness, hydrophilicity, surface energy and protein absorption, and cellular responses to PEEK based composites for orthopedic applications, *J. Mater. Chem. B* 8 (2020) 2618–2626.
- [90] N. Yu, X. Wang, L. Qiu, T. Cai, C. Jiang, Y. Sun, et al., Bacteria-triggered hyaluronan/AgNPs/gentamicin nanocarrier for synergistic bacteria disinfection and wound healing application, *Chem. Eng. J.* 380 (2020), 122582.